Journal of Volcanology and Geothermal Research 370 (2019) 13–30

Contents lists available at ScienceDirect

Journal of Volcanology and Geothermal Research

journal homepage: www.elsevier.com/locate/jvolgeores

Understanding the isotopic and chemical evolution of Yellowstone hot spot magmatism using magmatic-thermomechanical modeling

Dylan P. Colón [a,*], Ilya N. Bindeman [a], Taras V. Gerya [b]

[a] Department of Earth Sciences, University of Oregon, Eugene, OR, USA
[b] Department of Earth Sciences, ETH Zürich, Zürich, Switzerland

ARTICLE INFO

Article history:
Received 15 July 2018
Received in revised form 2 December 2018
Accepted 6 December 2018
Available online 13 December 2018

Keywords:
Thermomechanical modeling
Oxygen isotopes
Hafnium isotopes
Hot-spot magmatism

ABSTRACT

Large-scale melting and reworking of the crust and the upper mantle occurs in areas of mantle plume-crust interaction, generating voluminous and bimodal basaltic and silicic magmatism. Continental hot spot track magmas preserve geochemical and temporal records of these processes. Here, we apply and further develop the large scale (crust and the upper mantle) I2VIS magmatic-thermomechanical modeling code to investigate the potential origins of chemical and isotopic trends in the Yellowstone hot spot track, perhaps the best studied and constrained subcontinental mantle plume system on Earth. We model the propagation of melt via dikes in solid crust and via percolation in partially molten crust by using Lagrangian markers which also track the chemical and isotopic compositions of the melts that eventually erupt at the surface. Confirming the results of earlier geophysical and geochemical studies, we show that the eruptive activity at Yellowstone is best explained in terms of the formation of a ~15 km-thick mid-crustal mafic sill complex with its top at a depth of ~8 km that develops over a period of ~3 Myr. This sill complex releases rhyolitic fractionates and creates additional rhyolites by melting the surrounding crust, driving the voluminous rhyolitic volcanism which characterizes the Yellowstone system.

We recognize three key trends in the evolution of a continental hot spot volcanic center such as Yellowstone: (1) frequent, small eruptions results in in larger erupted rhyolite volumes compared to rare and large eruptions, (2) erupted magmas tend to be initially comprised of a large degree of crustal melt, and the relative contribution of fractionates of basalts from the mantle increases with time, and (3), the initial depth of the crust which melts to produce eruptible rhyolites becomes shallower with time. The first of these trends is simply a function of the continuous supply of new basalt to the crust from the mantle. The latter trend, which is responsible for low-$\delta^{18}O$ rhyolites, is produced by a combination of progressive melting of shallower crust as the system becomes hotter, repeated caldera collapses advecting shallow crust to a depth where it can melt, and the overplating and burial of shallow crust by repeated intrusions of basalt. The mid- and lower crust is not a significant source of erupted rhyolitic melts, as both the crustal melting and basalt fractionation takes place in the sill complex which forms near the bottom of the upper crust. The resulting modeled isotopic evolution of erupted magmas are a good match with the actual stable and radiogenic isotopic record of Yellowstone hot spot track volcanism preserved in zircon phenocrysts, and further replicates the results of recent geophysical imaging campaigns, giving us confidence that the assumptions and results of these thermomechanical models are broadly correct.

1. Introduction

Silicic magma genesis plays a critical role in processes ranging from the evolution of continental crust to explosive volcanic eruptions. The post-Columbia River Basalt part of the Yellowstone hot spot track, which is one of the most voluminous concentrations of erupted rhyolite in the Cenozoic Era (Bonnichsen et al., 2008; Pierce and Morgan, 2009), has received renewed interest in recent years due to advances in microanalytical geochemical techniques, high-precision geochronology, high-resolution seismic imaging, and numerical modeling (e.g. Huang et al., 2015; Wotzlaw et al., 2015; Colón et al., 2018a). These studies have provided critical constraints on the source materials for the rhyolitic melts which fuel the majority of volcanism in the region, including melts of the Cenozoic upper crust, the Precambrian lower crust, and material ultimately derived from the Yellowstone mantle plume (e.g. Drew et al., 2013; Wotzlaw et al., 2015; Colón et al., 2018b). Concurrently, there has been rapid progress in constraining the timescales over which these magmatic systems develop prior to erupting, which have shown that the giant pre-eruptive magma bodies with volumes of

* Corresponding author.
E-mail address: dcolon@uoregon.edu (D.P. Colón).

https://doi.org/10.1016/j.jvolgeores.2018.12.003
0377-0273/

10^3 km^3 or more can be assembled in as little as a few kyr, but may also inherit materials, particularly zircon phenocrysts, which date back millions of years earlier in the systems' history (Watts et al., 2012; Stelten et al., 2013; Wotzlaw et al., 2014, 2015; Rivera et al., 2016, 2017; Szymanowski et al., 2016; Colón et al., 2018b). These systems contrast strongly with the cooler, wetter, and more slowly assembled voluminous silicic magmas associated with arc magmatism (Christiansen and McCurry, 2008; Wotzlaw et al., 2013). Together, these observations suggest that the magmatic systems that fuel Yellowstone hot spot track super eruptions are both geometrically and temporally complex.

1.1. Numerical modeling insight into magma petrogenesis

The modern subsurface structure of the Yellowstone volcanic system has recently been constrained by geophysical imaging (Yuan et al., 2010; Hopper et al., 2014; Farrell et al., 2014; Huang et al., 2015), which has revealed a large shallow magma body at depth of 5 to 15 km, underlain by a larger and more diffuse magmatic system at depths of 25 to 45 km. Further insight into the origins of this structure are best provided by forward numerical modeling, which has the potential to study the physical evolution of a hot spot magmatic system in both space and time in a way that is inaccessible other methods.

Computer modeling of magmatic systems has been an active field of research for several decades now, with important insights provided by models of varying levels of sophistication. Much has been learned from one-dimensional and quasi-two-dimensional (e.g. axisymmetric cylindrical) models of magma genesis (Huppert and Sparks, 1988; Dufek and Bergantz, 2005; Annen and Sparks, 2002; Annen et al., 2006, 2015). These models continue to yield new results (e.g. Karakas et al., 2017) especially when coupled with analytical solutions for the stress fields controlling transport into and out of magma bodies by dikes (Jellinek and DePaolo, 2003; Karlstrom et al., 2009). More complex thermomechanical treatments of specific magmatic processes at various scales and resolutions including the emplacement and convection of melts and the elastic response of the surrounding crust have also been performed (e.g., Gerya and Burg, 2007; Simakin and Bindeman, 2012; Schubert et al., 2013; Keller et al., 2013; Gregg et al., 2015; Cao et al., 2016). These approaches provide high spatial and temporal resolution and allow good control in an investigated parameter space, but also only consider intrusive or eruptive events over scales of 1000s of years or less. At the other end of the spectrum, there have been several recent regional-scale thermomechanical models of mantle plumes and plume-crust interactions that do operate on the scale of many Myr (e.g., Burov and Guillou-Frottier, 2005; Burov et al., 2007; Sobolev et al., 2011; Burov and Gerya, 2014; Gerya et al., 2015), but have lacked or used very simplified magmatic processes treatments.

The rapid development of computational resources has allowed the combination of these regional-scale models with more sophisticated models of magma genesis in the crust. A recent such attempt was our previous study (Colón et al., 2018a), which used a magmatic-thermomechanical modeling code modified from the I2VIS code of Gerya and Yuen (2003). This study is the result of an attempt to bridge the gap between small and detailed models of individual phenomena such as advective heat transport (e.g. Annen and Sparks, 2002; Karakas et al., 2017) or dike propagation (e.g., Jellinek and DePaolo, 2003) with regional-scale models of tectonomagmatic systems such as mantle plumes which lack a detailed treatment of crustal magmatic processes (e.g. Gerya et al., 2015). In that study, we assumed that the primary mechanism by which rising magmas stall and accumulate in the crust is the trapping of dikes by rheological discontinuities in the crust, particularly the brittle-ductile transition that occurs at depths of 5–10 km. Based on this new model, we showed that the dominant control on the distribution of magma in the crust under Yellowstone is the presence of a large mafic sill complex that forms at depths of 10–20 km in response to this brittle-ductile transition, providing both heat and material to the magma bodies above and below it, corroborating observations of a similar feature under the eastern Snake River Plain which presumably dates back to the age of eruptions there (Peng and Humphreys, 1998).

In this new study, we seek to expand upon our previous results by improving the treatment of melt propagation through the crust and including simple methods for tracking the chemical and isotopic evolution of erupted melts. We check some of these results by using a simple modification of the cylindrical axisymmetric Heat2D code of Annen et al. (2015) which allows crustal melts to be erupted at the surface. Finally, we compare these results to observed geochemical trends in the eruptive products of Yellowstone hot spot volcanoes, in particular testing previous hypotheses concerning the origin of the enigmatic low-δ^{18}O and low-$\varepsilon_{Hf}/\varepsilon_{Nd}$ magmas which are found in great abundance throughout the hot spot track (Hildreth et al., 1984; Nash et al., 2006; Watts et al., 2011; Boroughs et al., 2012; Loewen and Bindeman, 2015; Colón et al., 2018b).

2. Geochemical trends in Yellowstone hot spot silicic calderas

We seek to understand the origins of the rhyolites that fueled the giant eruptions which have taken place along the Yellowstone hot spot track over the last 15 Myr (Fig. 1; Pierce and Morgan, 2009). To properly constrain our models, we turn to several important trends which have been identified by previous workers in both the isotopic and chemical compositions of the erupted magmas. Understanding these geochemical trends is important for evaluating our different models of the sources of erupted magmas, so we describe them here in some detail.

2.1. Chemical and thermal evolution of erupted rhyolites

The Yellowstone hot spot track is characterized by a pronounced Daly gap, with all erupted lavas and tuffs during the main phase of activity being either basaltic or rhyolitic in composition, with intermediate

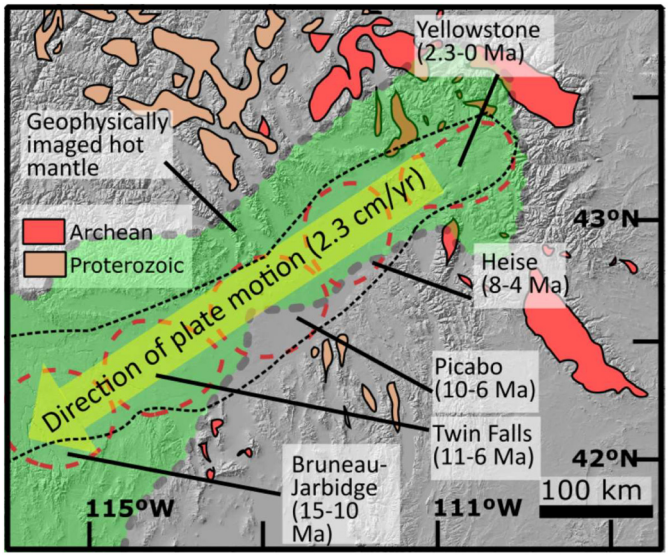

Fig. 1. Map of the Yellowstone hot spot track in continental North America, showing 15 Myr of magmatic activity. Red dashed ovals are the major named eruptive centers of the hot spot track (Bonnichsen et al., 2008), culminating in the site of modern activity at Yellowstone, which has been active since the last ~2.3 Myr. The green shaded area is the area where hot, seismically slow mantle has been imaged under the continental lithosphere, which has been interpreted as the remnant of older parts of the plume currently located under Yellowstone (Wagner et al., 2010). Solid orange and red represents areas of exposed Precambrian rocks in the region, of Proterozoic and Archean age, respectively (Barton et al., 2003), which are likely the source for the rare extremely low-ε_{Hf} magmas which occur on parts of the hot spot track. By contrast, voluminous low-δ^{18}O magmas have been found at every single part of the hot spot track. (For interpretation of the references to color in this figure legend, the reader is referred to the web version of this article.)

melts nearly absent (Christiansen 2001; McCurry et al., 2008; Szymanowski et al., 2015). Furthermore, the caldera systems themselves are almost exclusively rhyolitic, with basaltic eruptions limited to the margins of the system or the post-caldera phase of activity after the silicic magma bodies have presumably cooled and crystallized (Christiansen, 2001; McCurry et al., 2008). Hydrous phases such as amphibole and biotite are almost always absent, and calculated temperatures based on zircon saturation, and oxygen isotope phenocryst thermometry are typically above 800 °C at Yellowstone (Loewen and Bindeman, 2016; Troch et al., 2017). Along with the highly welded nature of most Yellowstone hot spot tuffs, this indicates that Yellowstone rhyolites are frequently very hot and dry compared to arc magmas (e.g. Branney et al., 2008). This is even more pronounced in the central Snake River Plain, where Ti-in-quartz thermometers in very crystal-poor magmas suggest temperatures approaching 1000 °C (Honjo et al., 1992; Cathey and Nash, 2009), and melting experiments suggest that observed mineral assemblages are produced at temperatures above 900 °C with H_2O contents not exceeding 2% (Almeev et al., 2012). Despite this, a few rhyolites contain up to 6% water with temperatures as low as 720 °C, most notably the Arbon Valley Tuff, which is coincidentally also one of the most low-ε_{Hf} magmas in the hot spot track, erupted at the start of the Picabo cycle (Drew et al., 2013, 2016). Silica content and temperature trends in Yellowstone hot spot magmas are not consistent across the hot spot track, with both cooling trends with increases in silica (Watts et al., 2012; Loewen and Bindeman, 2015) and heating trends with increasingly mafic magmas (Bonnichsen et al., 2008) observed at Yellowstone and the central Snake River Plain centers (Bruneau Jarbidge and Twin Falls), respectively. In contrast, there are common systematic changes in both the radiogenic and stable isotope compositions of the erupted rhyolites.

2.2. Radiogenic isotopes

Sr, Pb, Nd, and Hf isotopes clearly differentiate ancient Precambrian crust from material which has been extracted from the mantle more recently. Most rhyolitic magmas on the Yellowstone hot spot track have radiogenic isotope compositions between those of ancient crust and the mantle, indicating that they are derived from a combination of basalt fractionation and crustal melting (Nash et al., 2006; Shervais et al., 2006; McCurry and Rodgers, 2009). All the radiogenic isotope values along the hot spot track vary significantly between different eruptions, or even parts of one eruption, indicating that the relative contributions of crustal melts and mantle differentiates also vary greatly (Doe et al., 1982; Nash et al., 2006; Shervais et al., 2006; Watts et al., 2012; Drew et al., 2013; Colón et al., 2015a). The largest dataset available is for Hf isotopes, as Hf partitions strongly into zircon and is easily measured by in situ methods (e.g. Fisher et al., 2014). Most magmatic zircon from the hot spot track have Hf isotope compositions reflecting moderate involvement of unradiogenic crustal melting, clustering around ε_{Hf} values of −10 (Colón et al., 2018b), in line with the bulk-rock values of most major tuffs from the Snake River Plain (Nash et al., 2006; Colón et al., 2015a). More rarely, some units have extremely unradiogenic Hf isotopes, with ε_{Hf} values ranging from −25 to as low as −38, including the Arbon Valley Tuff at the Picabo Center (Drew et al., 2013, 2016) Huckleberry Ridge Tuff C at Yellowstone (Doe et al., 1982; Wotzlaw et al., 2015), and the Johnstones Camp Rhyolite at Bruneau-Jarbidge (Colón et al., 2015b). These low-ε_{Hf} magmas can only be produced by the melting of Precambrian crust, which is also indicated by the presence of xenoliths and xenocrysts with ε_{Hf} values as low as −60 in Snake River plain rhyolites (Leeman et al., 1985; Watts et al., 2010; Colón et al., 2018b). There is also significant evidence for the melting of much younger rocks such as the Idaho Batholith, Challis volcanics, and Paleozoic sediments, which have significantly more mantle-like radiogenic isotopes (Gaschnig et al., 2010; Boroughs et al., 2012; Colón et al., 2018b).

Previous studies have documented a trend of gradually increasing ε_{Nd} and ε_{Hf} values with time at each center, moving towards more radiogenic (mantle-like) compositions (Hildreth et al., 1991; Nash et al., 2006; Colón et al., 2018b). Recently Stelten et al. (2017) found a similar trend on a smaller scale, showing that the Central Plateau Member rhyolite lavas at Yellowstone also became gradually more radiogenic in their Hf isotopes with time, which they interpret as the result of the continuous input of isotopically primitive material from the mantle into the parent magma body. Notably, only one rhyolite with a significant population of these very unradiogenic zircon has been found at each major eruptive center, and they always occurred very early in the eruptive sequence at each center (Colón et al., 2018b). The trend of extremely low-ε_{Hf} material being erupted early in each volcanic center's evolution has been interpreted by Colón et al. (2018b) as possibly being the result of early melting of ancient deep crust followed by the isolation of the shallow crustal magma reservoir that fuels the large rhyolitic eruptions by a growing cumulate pile and mafic sill complex which separates it from the isotopically ancient deeper rocks. In this study, we seek to test these models and to consider which crustal compositions and structures yield the observed trends.

2.3. O isotopes

The Yellowstone hot spot track has long been recognized as the largest known concentration of low-$\delta^{18}O$ rhyolites in the world, with at least 10^4 km^3 of low-$\delta^{18}O$ tuffs and lavas having erupted in the last 14 Myr (Bindeman and Valley, 2001; Bonnichsen et al., 2008; Watts et al., 2011; Boroughs et al., 2012; Drew et al., 2013). Low-$\delta^{18}O$ magmas can only be derived from the melting of shallow, hydrothermally altered crust, with low-$\delta^{18}O$ being defined as anything less than the mantle value of +5.5–6.0‰ (VSMOW), with normal rhyolites ranging towards the higher part of this range because of minor isotopic effects during fractional crystallization (Taylor and Sheppard, 1986). Every major center in the Snake River Plain contains low-$\delta^{18}O$ rhyolites with values reaching as low as −2.6‰ in zircon phenocrysts, and whole-rock values as low as 0‰ (Bindeman and Simakin, 2014; Colón et al., 2018b). The caldera centers of the hot spot track in the Snake River Plain and Yellowstone (Fig. 1) also all exhibit a crude trend towards lower $\delta^{18}O$ values in erupted rocks through time, with the Picabo, Heise, and Yellowstone centers in particular opening with normal-$\delta^{18}O$ rhyolites and finishing at low-$\delta^{18}O$ values (Bindeman and Valley, 2001; Watts et al., 2011, 2012; Drew et al., 2013). By contrast, the central Snake River Plain caldera centers (Bruneau-Jarbidge and Twin Falls, Fig. 1) have initial eruptions which are low-$\delta^{18}O$, though still-lower values appear later in time, suggesting that the same trend of lowering $\delta^{18}O$ is at work there, if less clearly (Boroughs et al., 2012; Bindeman and Simakin, 2014; Colón et al., 2015a).

Attempts to understand the origin of the voluminous low-$\delta^{18}O$ rhyolites at the Yellowstone hot spot track have been a source of considerable recent debate. In summary, there have been 3 main proposed mechanisms for the production of low-$\delta^{18}O$ rhyolites: (1) intracaldera tuffs and lavas are hydrothermally altered in systems similar to that seen at Yellowstone today, making them low-$\delta^{18}O$, and further overlapping caldera collapses bring this material down to depths where it can be melted and re-erupted (Watts et al., 2011; Drew et al., 2013), (2) hydrothermal alteration along fault lines associated with tectonic extension related to the early stages of magmatism at each center produced low-$\delta^{18}O$ alteration of some combination of buried volcanic rocks, preexisting crust (such as the Idaho Batholith or Challis volcanics), and earlier hot spot-derived mafic intrusions, which later melted and produced low-$\delta^{18}O$ magmas (Drew et al., 2013; Colón et al., 2015a, 2015b; Blum et al., 2016;), and (3) older low-$\delta^{18}O$ alteration of the upper crust associated with earlier magmatism unrelated to the Yellowstone plume, such as the emplacement of the Idaho Batholith, provides pre-existing sources of low-$\delta^{18}O$ material for melting and eruption during Yellowstone plume magmatism (Boroughs et al., 2012; Ellis et al.,

2013), potentially explaining the fact that central Snake River Plain rhyolites are almost exclusively low-$\delta^{18}O$ in their composition. In any case, the trend away from mantle-like $\delta^{18}O$ values in erupted rhyolites at each caldera center stands in marked contrast with the evolution towards primitive values in radiogenic isotopes, which would suggest a role for some kind of crustal melting even at the latest stages of each system, but also that the type of crust which is melting changes distinctly. Understanding these trends is a key goal of this study.

3. Methods

3.1. I2VIS magmatic-thermomechanical models

We employ large-scale 2D marker-in-cell-based magmatic-thermomechanical finite difference models of the Yellowstone system modified from those of Colón et al. (2018a) to consider the evolution of a single part of the Yellowstone hot spot track. In Colón et al. (2018a), we modeled the interaction between a deeply-sourced mantle plume and overlying lithosphere which moves at 25 km/Myr relative to the plume. These models solve momentum (Stokes equation) and mass and energy conservation equations:

$$\frac{\partial \sigma'_{ij}}{\partial x_j} - \frac{\partial P_i}{\partial x_i} = -\rho g_i \tag{1}$$

$$\frac{\partial v_i}{\partial x_i} = \Gamma \tag{2}$$

In these equations v is velocity, P pressure, σ' is the deviatoric stress tensor, ρ is density, g is (purely vertical) gravitational acceleration, x_i are the spatial coordinates, and Γ is a source term that accounts for local melt extraction and emplacement. We couple these fluid-flow equations with a Lagrangian heat equation that includes radioactive, shear and adiabatic heating:

$$\rho C_p \left(\frac{DT}{Dt}\right) = \frac{\partial}{\partial x_i}\left(k\frac{\partial T}{\partial x_i}\right) + H_r + H_s + H_a \tag{3}$$

where T is temperature in kelvin, C_p is the heat capacity, k is thermal conductivity, H_r is radiogenic heating, which is a predefined constant, H_s is shear heating, and H_a is adiabatic heating/cooling. Latent heat of fusion is considered by modifying the heat capacity for partially molten materials (see Colón et al., 2018a). These equations are solved on a two-dimensional fully staggered finite difference grid and temperature advection is performed with markers. For this model, we use a 2 × 2 km square finite difference grid with 16 Lagrangian markers per cell at the start of the run (subject to change during material advection and melt extraction). For full discussion of the methods via which these equations and the terms within them are computed and solved see Gerya and Yuen (2003) and Gerya (2010), as well as additional notes in the Appendix for this paper.

3.2. Melt transport in the I2VIS model

We consider four main methods by which melt is transported in the crust and upper mantle, after Solano et al. (2012). (1), melt may be transported via dikes. This requires a relatively large volume of melt and rigid, mostly solid crust that can fracture. (2), areas of partial melt with sufficient permeability may allow the extraction and transport of melt through them via porous flow. The melt fraction threshold at which porous flow can occur varies depending on the rock composition and grain size, but we assume for these models that it can occur at melt volume fractions as low as 2% (Solano et al., 2012). (3), large melt bodies which are over 50% molten will internally convect and/or stratify. Finally (4), entire melt bodies or areas of partial melt may rise or sink as buoyant diapirs in thermally weakened lower crust and mantle (Keller et al., 2013).

Previous workers have mostly attempted to model these types of melt transport one at a time, as they take place on extremely different length and timescales (e.g. Ramberg, 1971;Kavanagh et al., 2006; Maccaferri et al., 2011; Solano et al., 2012; Keller et al., 2013; Bindeman and Simakin, 2014). To encompass the full behavior of the magmatic system under hot spot volcanoes, we undertook the task of considering all these melt transport phenomena simultaneously within a single computational run. The movement of diapirs (number 4 above) is slow enough that it is captured by the bulk physics of our models (Eqs. (1)–(3)), but diking, porous flow, and internal convection require modeling techniques beyond the simple Stokes flow equations discussed above, as they occur on temporal and spatial scales which are much smaller than the 5 kyr timestep and 2 km grid size of our model. For simplicity, we assume that all melt that originates in the mantle intrudes in the crust as dikes, as we are not concerned with the structure of any intrusions in the upper mantle for this study. We also make the major assumption that all melt transport of the first three types is purely vertical, to make the physics much more tractable.

For melt extraction, we consider the melt fraction of each Lagrangian marker in the model based on their composition, temperature, and pressure (there are initially 16 such markers per 2 × 2 km cell). For markers with >50% melt fraction, we consider two melt transport regimes, which are defined by whether eruptions are permitted. Eruption triggering mechanisms in large caldera-forming systems are poorly understood and depend on many parameters (e.g. Allan et al., 2012; Gregg et al., 2015; Karlstrom et al., 2012), so we consider their occurrence to be random for the purposes or our models. A random number generator gives each time stop an equal probability of having an eruption, and we adjust the probabilities to give the desired average recurrence interval. If an eruption is determined to be occurring by this method, we transport all markers in the crust that are at least 50% molten to the surface if they are buoyant enough for this to be possible (we consider all felsic magmas to have densities of 100 kg/m^3 during eruptions due to volatile exsolution for this purpose, making them almost always buoyant enough to erupt). If eruptions are not occurring, markers with a melt fraction that exceeds 50% initiate a dike, which proceeds vertically upward and produces a distribution of new melt markers via the method described in detail in Colón et al. (2018a) and the Appendix accompanying this paper. In this dike emplacement method, we use the non-dimensional value D:

$$D = \frac{\Delta P}{\eta}\Delta t \tag{4}$$

where ΔP is the magma overpressure in the dike (defined as the difference between the hydrostatic pressure in the dike and the ambient pressure as calculated in Eqs. (1)–(2)), η is the viscosity of the host material, and Δt is the time step, computed in the entire vertical column over the source melt marker where ΔP > 0 (where the magma is buoyant). D is computed over the entire column of material in which melt is buoyant enough to continue to rise, and dikes give rise to sills when they cross local maxima in this D value, caused by high buoyant overpressure and/or weak surrounding crust. The fraction of available melt which is trapped by a given local maximum in D is computed as follows:

$$\textit{intrusion fraction} \propto \left(\frac{D_{max}}{D_{min}}\right)^{0.5} \tag{5}$$

where D_{max} is the value of D at the local maximum in question, and D_{min} is the value of D at the overlying local minimum along the same purely vertical dike. The 0.5 exponent is used to improve numerical stability and prevent runaway intrusion at only one depth (Colón et al., 2018a). In addition to intrusion at local maxima of D, 20% of all available melt along a dike is also evenly distributed along the entire length of the

dike within the crust (see Colón et al., 2018a). Finally, a key difference in this model from the work of Colón et al. (2018a) is that dikes are allowed to have a crystal cargo, and both the melt and crystal parts of Lagrangian markers which are >50% melt are transported in dikes.

If the melt fraction of the marker is between 2% and 50%, it cannot feed eruptions, but can still be transported via porous flow up or down vertically, as long as the average melt content in its local 2 × 2 km cell is above 2%, and the melt cannot propagate into cells which contain <2% partial melt. This choice of threshold follows the work of Solano et al. (2012), and changing it does not significantly affect outcomes, especially early in each model's evolution. In this case only the liquid part of the original marker moves and it seeks its level of neutral buoyancy. Rising dikes that encounter zones of at least 20% partial melt will also only continue if they are still buoyant relative to the surrounding material, allowing bodies of evolved magma to form buoyancy traps for underplating dense mafic magmas. This behavior is unique to this study and is also not considered in the results of Colón et al. (2018a). While the 2 km grid resolution of this model clearly exceeds the volume of individual dikes and sills, we feel that this resolution adequately captures the large-scale rheological features in the crust which trap rising melts, without excessively exaggerating the melt-trapping power of very small local contrasts in rock strength due to individual fractures or other weak zones, as can happen at very high resolutions (<0.5 km grid size) without slight modifications to Eq. (5), which are still under development.

Finally, in Colón et al. (2018a), we limited the amount of melt from a given marker intruding into a cell above it so that the volume of each new marker V_{int} (there may be many such markers per cell) could not exceed the value $D^*V_{source\ marker}$ for that cell, in an attempt to limit excessive intrusions into cold and brittle crust. We do not employ this functionality in this study as its effects appear to be not well characterized and can lead to unwanted feedbacks in the context of Eq. (5), causing melt to be trapped in the lower crust and not advance to shallower levels. For a detailed treatment of the methods by which melt extraction is treated in the model see the Appendix.

3.3. Isotopic modeling

We also track the isotopic compositions of Lagrangian markers, both molten and solid. Given the large $\delta^{18}O$ ranges of different components in our systems, we assume for simplicity that there is no noticeable fractionation in oxygen isotopes during fractional crystallization or partial melting, at least relative to the large changes in $\delta^{18}O$ values which can be derived from hydrothermal alteration of the crust (Bindeman, 2008). Similarly, Hf isotopes are completely unchanged during melting and melt extraction, but can mix as markers melt and advect. We assume that all hydrothermal alteration (lowering the $\delta^{18}O$ of rocks/markers) occurs in the uppermost crust in heated areas, which have been additionally mechanically disturbed in some way, presumably opening fractures which allow the circulation of low-$\delta^{18}O$ meteoric waters. We consider areas in the upper crust which have been weakened by strain (effective viscosity of $<10^{22}$ Pa·s) to be vulnerable to penetration by meteoric waters and thus hydrothermal alteration (e.g., Gottardi et al., 2013; Colón et al., 2015b). Lower (Precambrian) crust is assumed to be impermeable, and thus not prone to alteration. We also require a heat supply, and only allow hydrothermal alteration to occur in a temperature window of 100–300 °C, above which we assume that the ductile behavior of hot rocks and silica precipitation from solution closes pores and limits permeability. At T < 100 °C, we assume low-$\delta^{18}O$ rocks cannot form because the fractionation factors between fluids and rock become large, making equilibrium rock values high rather than low in $\delta^{18}O$ (Taylor, 1968). Finally, we require that hydrothermal alteration only occurs in areas where an enhanced geothermal gradient can drive circulation of fluids, with values of at least 40 °C/km. Without this final requirement, we observe extensive hydrothermal alteration of the crust in areas where it is likely inappropriate, such as faults in relatively cold crust with no magmatic activity of any kind nearby. If these criteria are satisfied, we automatically reset the $\delta^{18}O$ value of a marker to −8‰, suggesting equilibration at high temperature with very low-$\delta^{18}O$ meteoric waters (e.g. Troch et al., 2018). We do not set a maximum depth for alteration in the code, but this seems unnecessary considering our results (see discussion).

3.4. Heat2D modeling

We modify the Heat2D code of Annen et al. (2008) to allow eruptions at periodic fixed intervals. This is a pseudo-2D axisymmetric model designed to mimic the conditions of the I2VIS models (see below). Intrusions of basalt at a fixed depth displace all surrounding felsic crustal material downwards. During time steps where there are eruptions, crustal material which is at least 50% molten is evacuated to the surface, while partial melts of mafic intrusions are not erupted, due to the difficulty of separating the liquid and solid parts of partially molten rocks in the purely thermal model. Any material above the removed molten material is advected downwards until any resulting gaps are filled, in an extremely simplistic analog of caldera collapse. We use these models to test some of the observations made in the thermomechanical models in a simpler geometry, particularly observations of the relationship between eruption repose times and total cumulative eruptive volumes.

4. Model setup

We use the same 1000 km × 300 km model space with a regularly-spaced 2 × 2 km finite difference grid as in Colón et al. (2018a), with a mantle plume generated by a thermal and advective boundary condition anomaly at the center of the base of the model. In our standard model, the continental crust is initially 35 km thick with 5 km of upper crust and 30 km of lower crust. This closely reflects the crustal structure used in the standard model in Colón et al. (2018a), modified slightly to reduce the thickness of the uppermost crust to better reproduce the observed isotopic trends (see Appendix). The upper crust (Fig. 2, brown) is assumed to be rheologically weak (wet quartzite law of Ranalli, 1995), to have a low solidus temperature characteristic of granite or sediment melting in the presence of fluids, either from their own hydrous minerals or from fractionating basalts (Johannes, 1985; Poli and Schmidt, 2002), to have a silica content of 70 wt%, a density of 2700 kg/m^3 (all densities reported for atmospheric temperature subject to compressibility at depth), and an ε_{Hf} value of −10 (Gaschnig et al., 2010; Colón et al., 2018b). The top 2 km of lower crust (Fig. 2, orange) is identical to the upper crust in every way (high silica, fertile, not dense), except for the fact that it has an ε_{Hf} value of −60, which matches the most isotopically ancient xenoliths and xenocrysts found in the Snake River Plain so far (Watts et al., 2010; Colón et al., 2018b). We assume that it has a low solidus temperature like the upper crust, but we also assume that >30% melt extraction by volume converts this lower crust to a dry mafic cumulate, which is not the case for upper crust, making it somewhat less fertile than the upper crust. The rest of the lower crust (gray) follows the dry mafic melting curve of Hess (1989; see Fig. 3), the An75 rheology of Ranalli (1995), and has a silica content of 50%, a density of 2900 kg/m^3, and an ε_{Hf} value of −60. The lowermost 5 km of crust above the Moho is a mafic cumulate assumed to have the same properties as the main part of the lower crust, but is slightly denser (3000 kg/m^3) and has only 45% silica. The mantle also has 45% silica and a density of 3000 kg/m^3, follows the dry olivine rheology of Ranalli (1995) and the dry mantle melting scheme of Katz et al., (2003), and has an ε_{Hf} value of a +5. For further information on material properties see Colón et al. (2018a). We initially set all crustal material to have a normal $\delta^{18}O$ value of +7‰ and all mantle to have a $\delta^{18}O$ value of +6‰.

The initial Moho temperature is 700 °C, with a geothermal gradient of 35 °C/km in the top 15 km of the crust overlying a much shallower

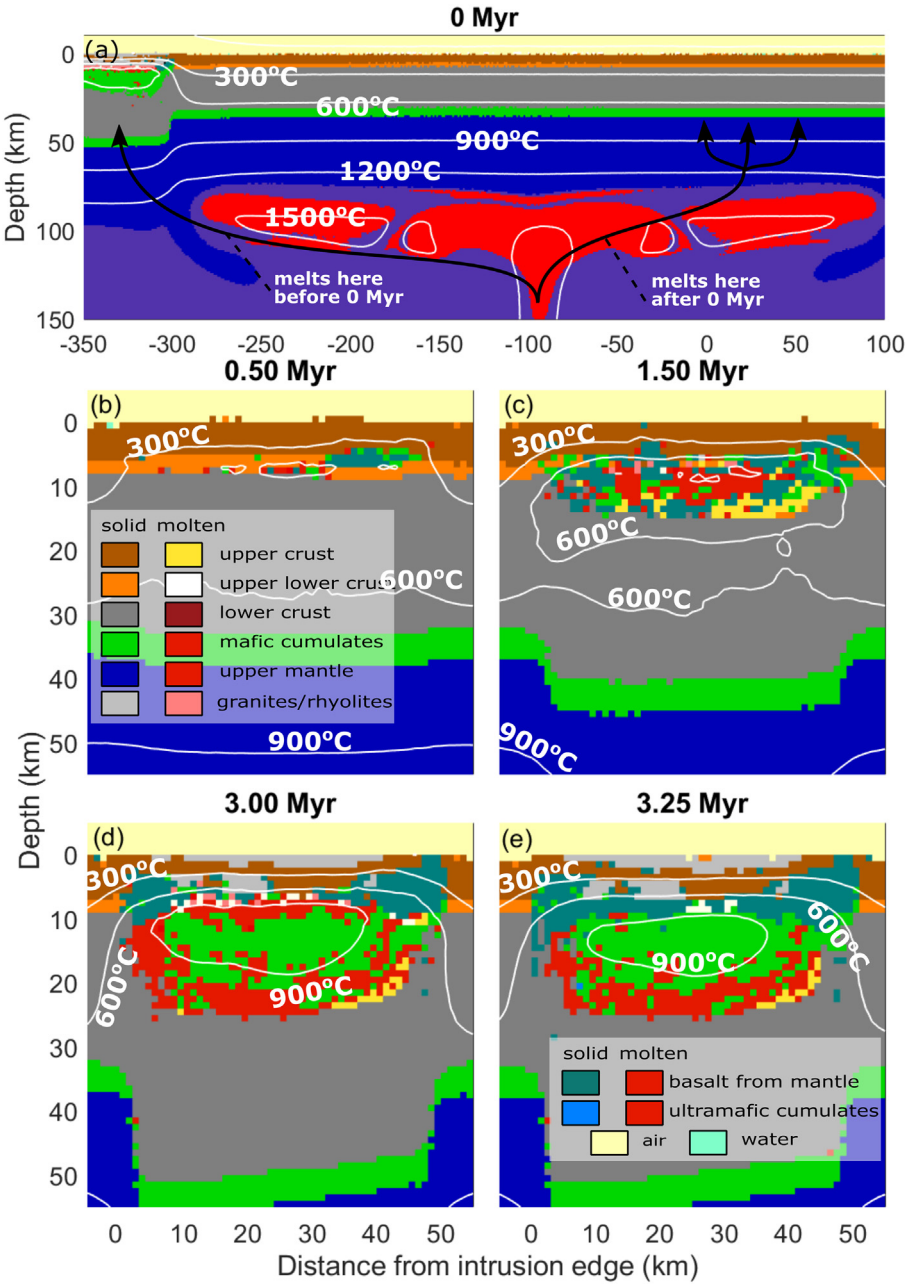

Fig. 2. Development of the Yellowstone magmatic system in the I2VIS model. (a) After an initial 2 Myr period during which the mantle plume is allowed to mature as a melt source, melts it produces are diverted towards the target area at the base of the crust along the line from 0 to 50 km on the x-axis, after which it ascends naturally. Intrusions gradually build a large mafic sill complex (b–d), which remains partially molten while basalt intrusions continue. After the intrusion rate drops by 90% after 3 Myr, the sill complex cools and solidifies rapidly (e). Note that the position of the top of the intrusive complex remains relatively constant at 5–6 km, while its bottom reaches progressively deeper depths as new magma intrudes, advecting the lower crust downward and thickening the crust. At the top of the sill complex and at the surface, significant volumes of granitic intrusions and erupted rhyolites (both light gray), respectively, form from both crustal melting and fractionation of the large partially molten sill.

geothermal gradient in the initial model setup. This rapidly equilibrates to a nearly linear 20–25 °C/km gradient over the entire crustal column in the 2 Myr period during which the model is allowed to run before magmatism begins, even in the presence of radiogenic heating in the upper crust. Below the crust is 45 km of mantle lithosphere, producing a lithosphere-aesthenosphere boundary at 80 km depth, as constrained by the modeling of Colón et al. (2018a). These mantle layers differ only in their initial temperature gradient and are otherwise identical. The asthenosphere has an initial adiabatic temperature gradient of 0.5 °C, with a potential temperature of 1350 °C; the aesthenospheric temperature gradient connects this with the crustal geotherm (Fig. 2a). The mantle plume is 175 °C hotter than the surrounding mantle, as was constrained in Colón et al. (2018a).

Unlike in the previous Colón et al. (2018a) study, which primarily focused on interpreting/recreating geophysical images of the Yellowstone system, we are mostly interested in the isotopic and chemical evolution of magmas at any given single eruptive center along the hot spot track. We compensate for the lack of horizontal melt transport (see above) by evenly distributing melts from the plume in a 50 km-wide zone of crust, after an initial 2 Myr of model time in which the plume is allowed to stabilize. During this initial time, melts from the plume are transported horizontally far away from the main 50 km-wide zone of intrusion, so that the crust at the start of intrusion there is initially undisturbed. After this transport to the base of the crust (Fig. 2a, black arrows), the melts are allowed to rise in a natural way that is governed by the methods described above and in the Appendix. This additionally allows

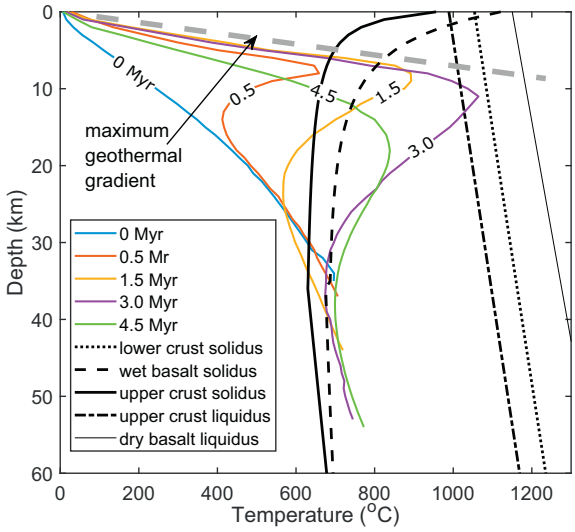

Fig. 3. Evolution of the geothermal gradient in the growing magmatic system shown in Fig. 2, showing the thermal effect of 3 Myr of basalt intrusion at a rate of 20,000 km^3/Myr. The initial geothermal gradient (blue) is approximately 20 °C/km, and produces a Moho temperature of 700 °C at a depth of 35 km. Basaltic magma intrusion focused at 7–8 km depth rapidly raises the temperature of the upper crust, initiating melting there after 0.5 Myr, when the solidus temperature of the upper crust is reached by the hottest part of the growing intrusions. Peak temperatures of approximately 1000 °C are reached inside of the differentiating mafic sill complex at depths of approximately 10 km after 3.0 Myr, after which basalt intrusion from the mantle ceases and the system begins to cool. This cooling is slow, however, and peak temperatures 1.5 Myr after basalt intrusions decrease to 2000 km^3/Myr are still >800 °C. Finally, we note that the geothermal gradient in the upper crust does not seem to ever exceed ~150 °C/km and that continued of crustal heating instead simply increases this high gradient's maximum depth. Liquidus and solidus curves are from Johannes (1985), Hess (1989), Schmidt and Poli (1998), and Poli and Schmidt (2002). (For interpretation of the references to color in this figure legend, the reader is referred to the web version of this article.)

for closer comparison with the Heat2D models, which have no crustal movement aside from the vertical movement associated with intrusions and eruptions. Intrusion continues in the 50 km-wide zone for 3 Myr, consistent with the lifespan of the two most recent caldera centers on the Yellowstone hot spot track at Yellowstone and Heise (Christiansen, 2001; Morgan and McIntosh, 2005).

The amount of melt which is intruded into the crust is fixed at 20,000 km^3/Myr, which if we divide by an assumed model thickness of 50 km, gives a basalt intrusion rate identical to that of the preferred model in Colón et al. (2018a). Crustal thickening is controlled entirely by intrusions, though it is somewhat counteracted by erosion at the surface and viscoplastic horizontal transport of material away from the intrusions. This is all in contrast with the simpler situation in the models of Colón et al. (2018a), where a ~25 km wide zone of intrusion and crustal melting moves at a velocity of 25 km/Myr, creating a very clear and uninterrupted trend in position versus eruption time on the surface of the hot spot track, but which does not linger long enough at any one point in the crust to produce the long-lived volcanic systems typical of the actual hot spot track. After 3 Myr of intrusion into the target zone seen in Fig. 2, melt is again diverted far away and the system cools, save for a residual long-lasting intrusion rate of 2000 km^3/Myr, 10% of the intrusion rate of the "peak" volcanic period.

5. Results

5.1. Development of the mid-crustal sill complex

In the new series of models employed here, we confirm the main result of Colón et al. (2018a), showing that basalts rising from the mantle primarily accumulate in a mid-crustal sill complex which occupies depths of 8–25 km by the time it has fully developed after 3 Myr of intrusions (Fig. 2d). Combined with other more diffuse intrusions in the lower crust, these produce a total of 15–20 km of crustal thickening (Fig. 2d), in line with or slightly higher than previous estimates for the Yellowstone hot spot track (McCurry and Rodgers, 2009; Yuan et al., 2010). However, this can be explained by the fact that this is compensated for by adjacent gaps in apparent magmatism, such as between Yellowstone and Heise, which can be filled in by lower crustal flow as the system evolves in a more realistic 3D model, allowing us to remain within existing geophysical and geochemical constraints on the Yellowstone system. Additionally, ~4 km of this material is deposited in a distributed manner in the lower crust and does not contribute noticeably to the sill complex or to volcanism, and instead heats the crust, and thus can be considered "missing" from mass balance assessments such as that of McCurry and Rodgers (2009). The depth of the top of this intrusive system corresponds to the brittle-ductile transition, which is the site of the greatest contrast in D (D_{max}/D_{min} is maximized, see Eqs. (4), (5)) and therefore traps the most rising melts. The mafic magmas of the sill complex drive rhyolite production through their fractionation to form rhyolitic residual liquids, and by heating and melting of the surrounding crust, which begins approximately 0.5 Myr after the start of basalt intrusion in our standard model (Figs. 2–5), when the crust at a depth of approximately 8 km first reaches its solidus temperature. With the exception of its uppermost 2 km (orange, Fig. 2), the lower crust is too refractory to melt, and melts there are fractionating basalts from the mantle rather than crustal partial melts (Figs. 2–4).)

5.2. Evolution of the geothermal gradient

The addition of mafic melts with temperatures as high as 1350 °C from the mantle plume into the crust causes extremely rapid heating of the upper crust, as is documented in Fig. 3. We start with a steady-state crustal geothermal gradient of ~20 °C/km in both the upper and lower crust, which stabilizes as such in our model despite having upper crust which is ~10 times as radioactive as the lower crust. 0.5 Myr after the beginning of basalt intrusion, temperatures at 8 km depth have already reached ~650 °C, allowing the first rhyolitic liquids to form (Figs. 3, 4a). This corresponds to the depth of the incipient sill complex formed by the earliest intrusions (Fig. 2b). By 1.5 Myr after the start of intrusion (Figs. 2c, 3, 4b), a broad region of crust from depths of 7–13 km depth is heated above its solidus temperature, releasing large quantities of melt, some of which erupts (gray material at the surface in Fig. 2c). The peak in crustal melting occurs at the end of the caldera cycle at 3 Myr when rapid intrusions of basalt end, and a very large and broad magma body occupies the upper crust spanning depths of 5–30 km, fueling voluminous volcanism at the surface (Fig. 4). A noteworthy result is that the upper crustal geothermal gradient stabilizes at approximately 150 °C/km for all depths above the melt zone, after an initial steeper ramping up in the top kilometer of crust. This geothermal gradient does not increase over time, and instead merely extends itself to greater depths as the system matures, eventually reaching peak temperatures of over 1000 °C at depths of approximately 10 km. This high temperature does not necessarily mean that the crust there is nearly pure liquid, as it has been depleted by repeated extractions of partial melt, and as such is dominated by mafic cumulates. The fact that the peak in temperature at the base of this gradient always occurs near the top of the developing basaltic sill complex (Figs. 2, 3) suggests that most intrusions of new basalt naturally overplate the older solidified ones near the top of the sill complex.

When intrusion drops to post-caldera levels after 3 Myr, the system immediately begins to cool, and further crustal melting and rhyolite production ceases almost instantly (Fig. 5). The silicic melts which have already formed, however, are able to persist for a long time as the system cools. The mid-crustal sill complex solidifies before the partially molten crust above and below it, especially in its center where it consists of highly depleted mafic cumulates, producing a noticeable amagmatic gap between the partially molten crust above and below it, as was previously observed in the models of Colón et al. (2018a).

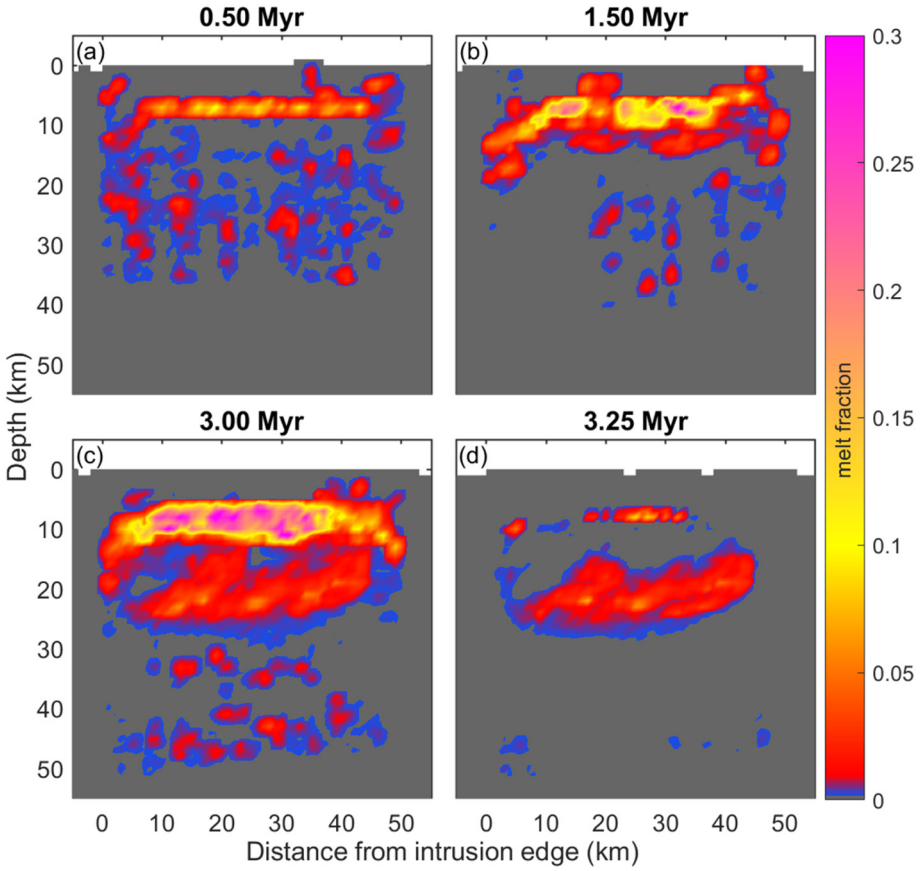

Fig. 4. Evolution of the melt bodies in our standard model. The views here are identical to Fig. 2. (a) At 0.5 Myr there are very small amounts of melt throughout the entire crust that represent rapidly cooling basaltic dikes, and a shallow magma body has begun to form at ~8 km depth. (b–c) Crustal melting and basalt fractionation rapidly accelerate until 3 Myr after intrusions start, when the total volume of melt in the crust is in excess of 2000 km^3. (d). After basalt intrusion drops by 90% after 3 Myr, the basaltic sill complex rapidly solidifies, but the lower crust and deepest sill complex below it remains partially molten where warm enough (see Fig. 3), and the rhyolitic magma body between 5 and 10 km depth also takes up to a million years to fully solidify.

5.3. Production of rhyolitic liquids

Rhyolitic liquids begin forming in the upper crust approximately 0.5 Myr after basalt intrusions begin when the temperature at the upper crust-lower crust boundary reaches the solidus. We plot a 75 kyr moving average of the production rates of different sources of felsic melts in the crust in Fig. 5 (reducing noise related to minor numerical issues). Melting of the upper 2 km of the lower crust, which melts according to the upper crustal solidus curve (Fig. 3), rapidly increases and peaks at ~1.3 Myr after the start of basaltic intrusions (Fig. 5). Lower crustal melting then plateaus and eventually declines as the material is depleted by the extraction of silicic melts. The main bulk of the lower crust does not contribute in any measurable way to the total volume of crustal melting, as it is too refractory (dry mafic melting curves in Fig. 3). Upper crustal melting does not begin until about 1.5 Myr after basalt intrusions begin, reflecting the considerable amount of energy required to heat such shallow rocks above their solidus temperature. Upper crust melts in increasing amounts until the caldera cycle ends, after which it abruptly ends, along with lower crustal melting. The greatest source of rhyolitic liquids by far, however, is the fractionation of basalt and the remelting of previously solidified basalt intrusions (with the latter being subordinate), meaning that while crustal melting is very important for producing Yellowstone hot spot tracks, most erupted material by volume is ultimately sourced from the mantle, even among the most evolved magmas. It begins at the same time as lower crustal melting, as before that basalts simply quench in the initially cold crust, and rapidly intensifies until basalt intrusion rates drop after 3 Myr. The final intrusion rate of 2000 km^3/Myr is not enough to produce new felsic liquids, even with the new higher geotherm (Fig. 3), and the system returns to erupting only basalts.

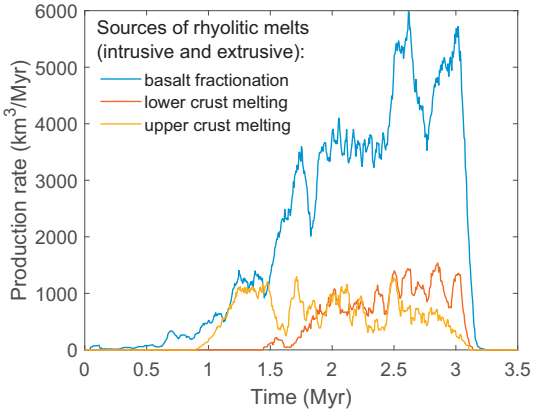

Fig. 5. Production rates of felsic liquids from basalt fractionation (including remelting of solidified basalt) lower crustal melting, and upper crustal melting. Basalt fractionation and lower crustal melting dominate the first 1.5 Myr of the system's evolution, after which lower crustal melting is replaced by upper crustal melting, while basalt fractionation becomes ever more efficient as the temperature of the system climbs. After 3 Myr, basalt intrusion rates drop from 20,000 km^3/Myr to 2000 km^3/Myr, and the system can no longer support significant rhyolite production due to a lack of heat, causing felsic melt production to rapidly cease in as little as 150 kyr after cooling begins.

5.4. Rhyolite production vs eruption rates as a function of frequency of eruption

We find that the total volume of erupted rhyolite depends heavily on the number of individual eruptions, with systems with more frequent

and total eruptions producing more material. This is seen by modifying the base model shown in Figs. 2–6 to change the average interval between eruptions from our standard model, where eruption repose times average 0.2 Myr. We see that systems with the average repose time set to 0.5 or even 1.0 Myr have much less total erupted rhyolite (Fig. 6a). For all cases, 0.2 Myr, 0.5 Myr, and 1.0 Myr repose times lead to a total erupted basalt volume of roughly 1000 km^3. When the average eruption repose time is instead decreased to 25 kyr, the amount of basalt that remains in the crust significantly decreases, as basalt passes to the surface in as many as a fifth of individual time steps, cooling the system and reducing rhyolite output (Fig. 6a, violet curve). However, if we take that same model and forbid basalt eruptions, we see a very large total rhyolite eruptive volume which no other model can match (green curve). This trend is despite the fact that longer repose times between eruptions are, intuitively, associated with greater eruptive volumes; this trend is more than counterbalanced by the greater number of smaller eruptions which occurs with smaller repose times. We further note that while total cumulative eruptive volumes strongly vary with eruption rates, the total volume of felsic melts produced (including intrusions) is less significantly affected by changing the eruption rate, with slightly higher total melt production occurring with longer repose times (Fig. 6b). Testing the source of this variation, we find that there is a noticeable correlation between the number of individual eruptions and the fraction of all felsic melts which erupt (Fig. 6c), and a very strong correlation between this ratio and the total eruptive volume (Fig. 6d).

To further test this observation, we employ the Heat2D models which, because of their relative simplicity, are easier to interpret. As described above, these models involve intrusions of basalt to a fixed depth (7 km in this case) with melting of the crust occurring purely via conductive heating from the sill. We erupt all crustal material with melt fractions of at least 50% at regular, nonrandom, intervals, but do not erupt partially molten basalt sills (see above). In the Heat2D models, 15 km of basaltic sills was intruded over a 2 Myr time period, with all new intrusions overplating the previous intrusions at a depth of 7 km, similar to what we observe in the model detailed in Figs. 2–4. Intruding basalts are assumed to have temperature of 1200 °C. Tracking the total volume of melt in the crust over time, we find that longer repose times are associated with significantly greater volumes of melt in the crust, including melt in both the basaltic intrusions (Fig. 7a), and in the partially molten surrounding crust (Fig. 7b). This is different from the total produced melt seen in Fig. 6b, as that adds all melt produced over the entire model history, which is harder to measure in the Heat2D models, whereas Fig. 7b simply plots the volume of melt present at any given time. Again, we find that larger repose times are followed by larger volcanic eruptions, with a maximum erupted volume of pure crustal melt of 1500 km^3 occurring in the case of a single giant eruption after 2 Myr (Fig. 7c). This increase in eruption size with repose time is not enough, however, to counter the decreased total number of volcanic eruptions, and we observe the same strong inverse correlation between total erupted volume over the lifetime of the system and the repose time between eruptions (Fig. 7d). We also compare the trend that we

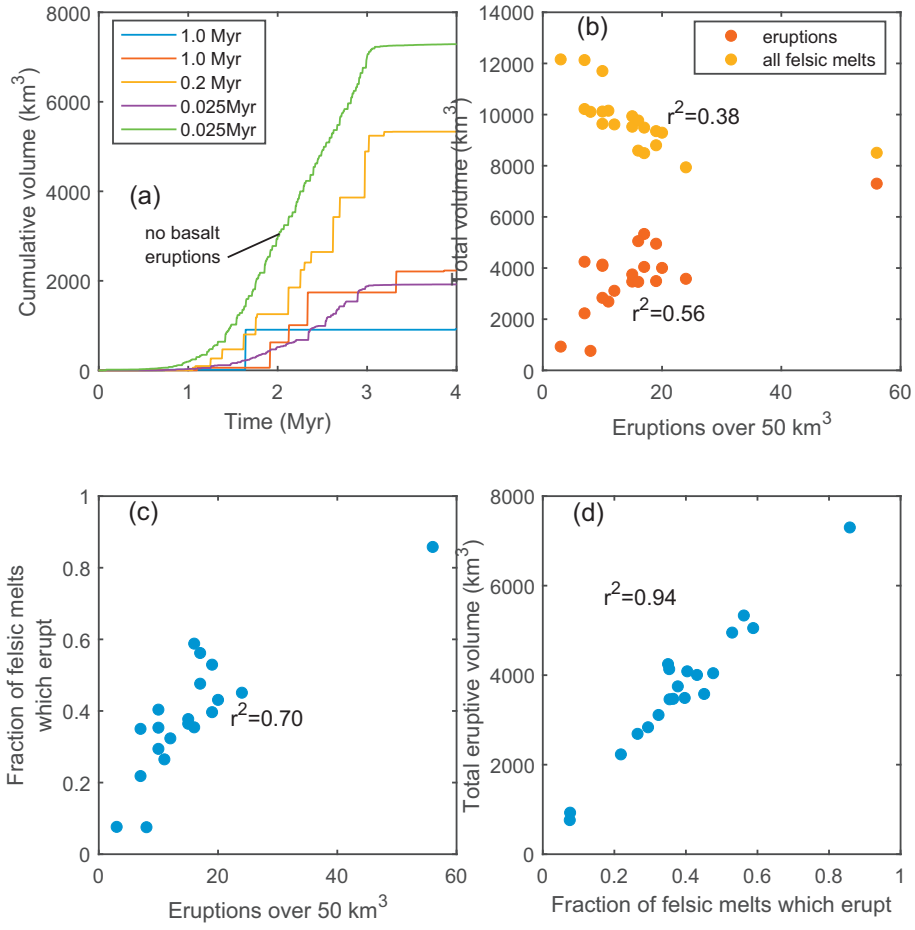

Fig. 6. (a) Plot of cumulative eruptive volume for simulations with different average repose intervals between eruptions. The yellow curve (0.2 Myr on average between eruptions, is our standard model. For the violet curve (average repose of 0.025 Myr) basalt eruptions are permitted, while for the green curve, they are forbidden. (b) Plot showing that an increased number of eruptions is associated with a greater total eruptive volume, but a lesser total volume of melts produced in the crust. Multiple data points are from repeated runs with the same initial conditions as models in (a). (c) Correlation between the fraction of felsic melts which erupt and the number of total eruptions with a volume of at least 50 km^3. (d) Correlation between the fraction of all felsic melts formed in the crust that erupt and the total cumulative eruptive volume. The model forming the violet curve in (a) is excluded from (b–d) because of its very different basalt/rhyolite ratio. (For interpretation of the references to color in this figure legend, the reader is referred to the web version of this article.)

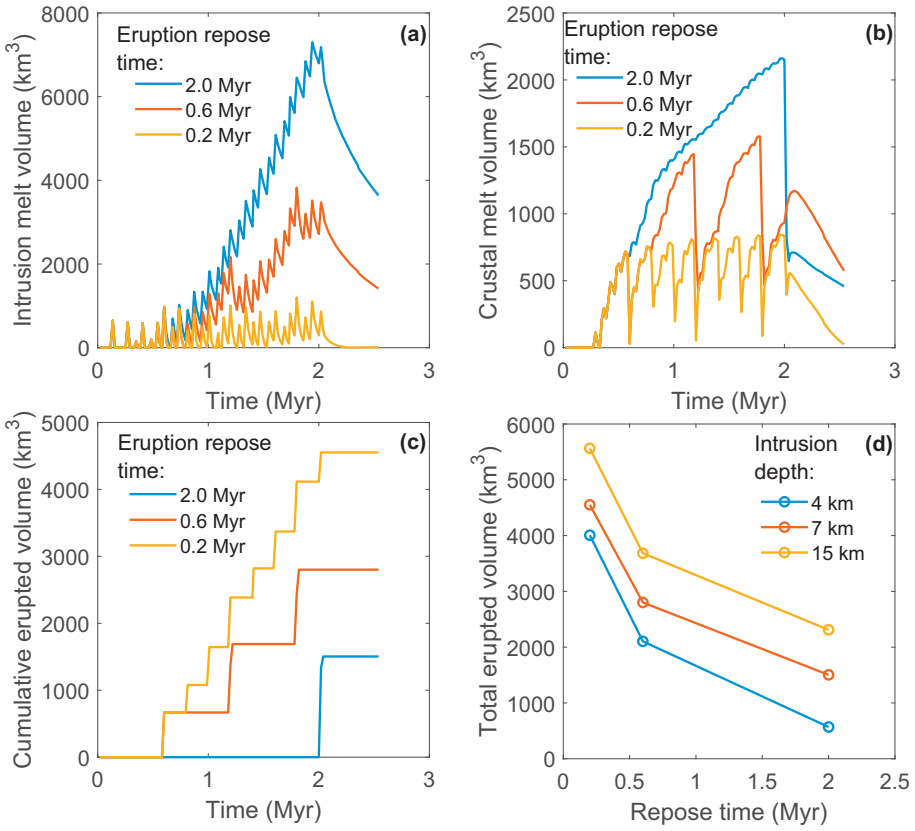

Fig. 7. Melt production in Heat2D assuming an initial geotherm of 20 °C/km, a sill accumulation rate of 7.5 km/Myr for 50 km diameter circular intrusions, which intrude overplating previous intrusions at 7 km depth (except for part d). (a) Total volume of partial melts in the mid-crustal sill, not including crustal melts. This material is not allowed to be erupted in these simulations, unlike in the I2VIS models. The total volume of melt steadily increases until 2 Myr, when new basalt intrusions are stopped and the system begins to cool. This increase is much greater in the models with less frequent eruptions. (b) Total volume of crustal melts in the system. This begins to rise approximately 0.3 Myr after the start of intrusions, as heating is more focused and efficient than in the I2VIS models because basalt intrusions always occur at the same level. The total melt volume drops when there are eruptions, but not to zero because partially molten areas with <45% melt cannot erupt. As with mafic melts, there is much more crustal melt at any given time in the models with infrequent eruptions. (c) Total erupted volume as a function of time, analogous to Fig. 6a. When eruptions occur more rapidly, they are smaller, but the total volume is larger. (d) Plot of total erupted volume, the final value in the part (c) curves, vs. the repose time, demonstrating the trend or greater total eruptive volume with more frequent eruptions. This trend is not affected by changing the intrusion depth, though the total volume is.

observe for intrusions at 7 km depth and find it nearly perfectly replicated when the basaltic intrusions accumulate at 4 km or 15 km depth, but with the expected increase in melting when the intrusions are at greater depths with higher ambient crustal temperatures, further confirming the robustness of this effect (e.g. Annen et al., 2006, 2015).

5.5. Variation in the width of the zone of intrusion

We also investigate the effect of varying the width of the intrusive zone in the crust from the 50 km that we assume for the model represented in Fig. 2. This is important because the width of the crust that is subject to basalt intrusions at any given time is not very well constrained. We suspect it is comparable in size to the calderas along the hot spot track, but even those vary from 30 to >90 km in length (Christiansen, 2001; Morgan and McIntosh, 2005; Pierce and Morgan, 2009). Testing this, we keep the total volumetric flux of basaltic melts from the mantle the same at 20,000 km^3/Myr and vary the total duration of the intrusion depending on the width of the system (Figs. 8–9). In this way, we fix the total amount of crustal thickening, but change the time and width of that thickening (width of zone on the right in Fig. 2a). This tests for uncertainty in the width of the plume and its footprint in the crust, while preserving the volumetric intrusion rate which was constrained in Colón et al. (2018a) for the modern Yellowstone system. This also allows us to investigate possible effects of having sills rising from individual dikes spread out over greater or lesser horizontal areas, which we cannot directly model in our code which only considers vertical melt transport.

We find that widening the zone of intrusion dramatically reduces the temperature of the crustal magmatic system (Fig. 8) and decreases the volume of both intrusive and erupted felsic melts (Fig. 9), despite the fact that the wider intrusions are allowed to accumulate for more time. In Fig. 9, we can clearly see that felsic melts are produced (and erupt) much more quickly in narrower intrusive settings with the same volumetric intrusion rate, and that the rate of melt production in wider intrusions never catches up even after the system thermally matures. This shows that four separate intrusive events that are 25 km wide and last for 1.5 Myr can be expected to produce far more melt than a single, 100 km wide distributed intrusive event that lasts for 6 Myr at the same volumetric intrusion rate. This allows us to put constraints on the width of the crust which is likely being heated at any given time by the Yellowstone plume, suggesting that in systems that are very laterally extensive, such as the roughly 100 km-long Yellowstone caldera complex, melt input from the mantle cannot be evenly distributed over the duration of the system and must be focused under different subsections of the volcano at any given time, otherwise the system would cool and fail to produce melts.

5.6. Isotopic trends in erupted rhyolites

The isotopic compositions of the erupted rhyolites in our thermomechanical models vary significantly over time, and broadly match many of the observations that have been made by previous workers for the volcanic products of the hot spot (e.g. Nash et al., 2006; Shervais et al., 2006; Watts et al., 2012; Drew et al., 2013;

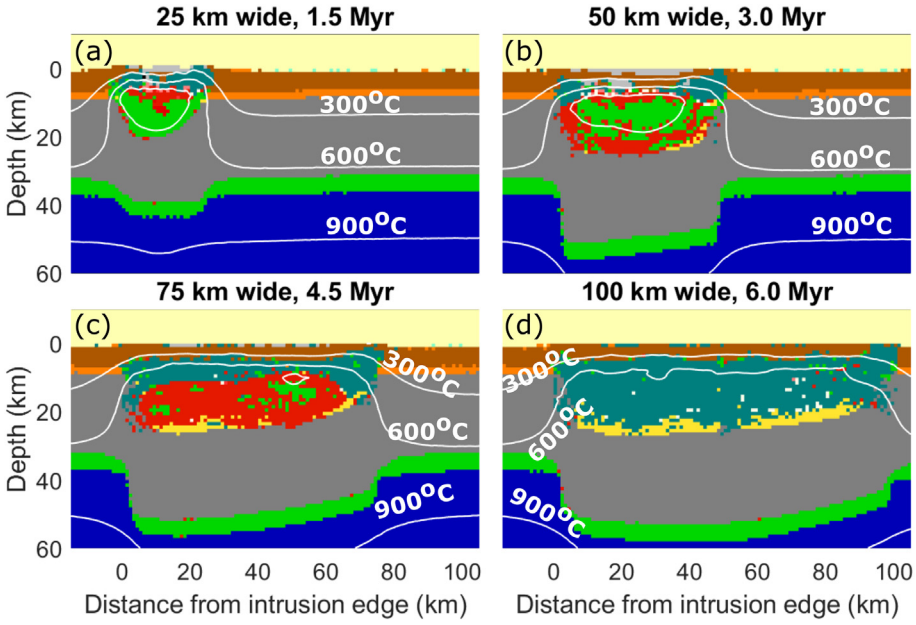

Fig. 8. Comparison of different intrusion widths. Models are compared at the end of the voluminous mafic intrusion time (varying between 1.5 and 6 Myr), which lasts longer for wider intrusions in order to obtain the same degree of crustal thickening given a fixed basalt intrusion rate of 20,000 km^3/Myr. Part (b) is identical to Fig. 2d. Note that with increasing width, the temperature in the center of the intrusion decreases. In part (a) it is over 1100 °C, while in part (d) the temperature at the center of the is only about 750 °C, even though heating of the crust continues for four times as long as in (a).

Wotzlaw et al., 2015; Colón et al., 2018b). Figure 10shows the evolution of the Hf and O isotopes both of the melts being produced in the crust at any given time (solid line) and of the eruptions themselves (open circles, scaled by eruptive volume). This demonstrates that the erupted rhyolites are indeed representative of what is beneath the surface at least in terms of the radiogenic isotopes. We see that the first major rhyolite eruptions have Hf isotope compositions which reflect the extensive melting of the lower crust (Fig. 10a), and that that signal later gradually recovers towards mantle-like values. This match is not as perfect with O isotopes (Fig. 10b), however, and where the erupted compositions are frequently considerably more normal-δ^{18}O than the melts which appear to be generated at the same time. This is likely because of the fact that the orange curve in Fig. 10b is calculated assuming that all upper crustal melts are low-δ^{18}O, which is not likely to be entirely true, and because the cool and shallow low-δ^{18}O melts that form in the crust may not typically reach the 50% melt threshold needed to erupt. That said, we do successfully reproduce the trend towards more depleted ^{18}O concentrations with time at Yellowstone.

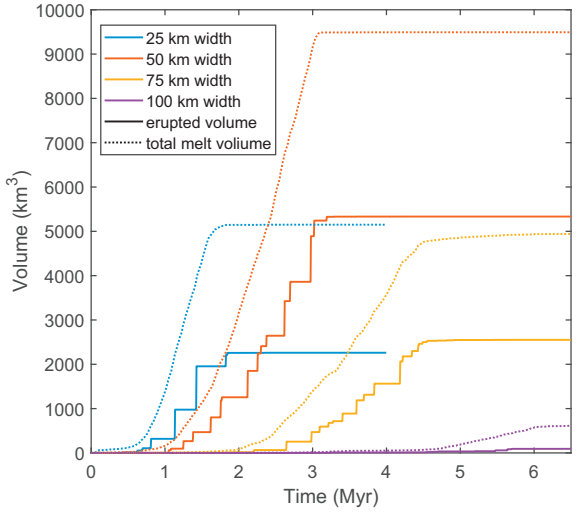

Fig. 9. Comparison of eruptive rates for the different intrusion width scenarios seen in Fig. 8. Significantly more felsic melt production (dotted lines), and therefore rhyolite cumulative eruption volume (solid lines), occurs when mafic intrusions are concentrated in a narrower region of the crust. Note that eruptions cease earlier for the narrow intrusion zone models, this is because the crustal thickening is achieved earlier, as the total mafic intrusion rate remains constant. Note the strong negative correlation between the rate at which felsic melts are formed and the width of the intrusion zone.

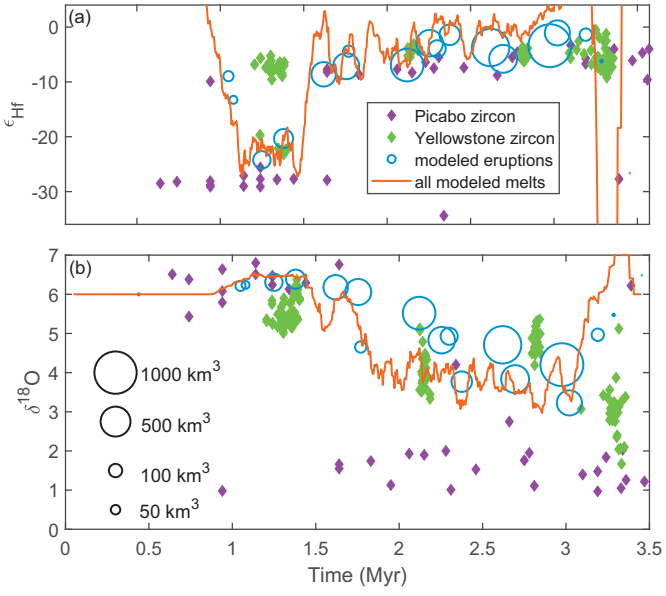

Fig. 10. Isotopic values of melts forming in the crust (solid lines) and the bulk values of individual eruptions (open circles). Diamonds are actual zircon isotopic compositions from the Yellowstone and Picabo centers (Colón et al., 2018b; Fig. 1). In the first 1 Myr, Hf isotpes (a) are extremely unradiogenic, indicating the melting of Precambrian crust, and O isotpes (b) of the erupted rhyolites are normal. As the system matures, Hf isotpes become much more mantle-like, while δ^{18}O values become more depleted, indicating the involvement of hydrothermal alteration of the crust followed by melting of that altered low-δ^{18}O material. Here zircon ages are normalized to match the age of the first eruption in the real world with the age of the first eruption in the model, all zircon ages are correct relative to each other for each system.

Fig. 11 shows us an alternate view of the isotopic trends, showing the stratigraphy of Hf and O isotopes for the up to 5 km-deep nested caldera system which develops at the surface in our standard model, which is visible as a thin gray layer at the surface in Fig. 2e. Fig. 11c clearly demonstrates that the low-$\delta^{18}O$ magmas are far from evenly distributed in the crust, and erupt preferentially from one part of the caldera. In the real world, these magmas would tend to homogenize with adjacent normal-$\delta^{18}O$ melts via horizontal convection, but this is not well-modeled in our code. This does suggest however that moderately low-$\delta^{18}O$ magmas are assembled in the crust from mixes of initial batches of more low-$\delta^{18}O$ magma (−2‰ or lower, see Colón et al., 2018b) and more mantle-like material. This is confirmed in the real world by the existence of moderately low-$\delta^{18}O$ rhyolites that are host to zircon crystals with $\delta^{18}O$ values which are several permil lower (Bindeman and Simakin, 2014; Colón et al., 2015a, 2018b; Watts et al., 2011.

5.7. Chemical and eruptive temperature trends in erupted rhyolites

Fig. 11b shows that the initial magmas to erupt in the system are almost exclusively basaltic magmas with low SiO_2 contents, and that after that basaltic eruptions are confined to the margins of the caldera system as it develops. Basalts in the center of the system either are trapped by the rhyolitic melt body and do not erupt or hybridize with the more silicic melts. We see that the part of the magmatic system which is producing the most upper-crustal melts as seen in the oxygen isotopes (left side, Fig. 11c), tends to be somewhat more felsic and less voluminous (shallower calderas) than the part that erupts more mantle-like crustal compositions. There is also a thin layer of basalt capping the caldera sequence which is the result of eruptions of basalt resuming in the caldera interior after the basaltic intrusion rate drops and rhyolite production stops. Fig. 12a shows that basalt eruptions dominate the beginning and end of the caldera life cycle, when there are fewer melt bodies in the crust to intercept them or drown them out through mixing. As the system heats, erupted rhyolites become more mafic with time, transitioning from high-silica rhyolites to low-silica rhyolites (orange circles, Fig. 12a). This trend is simple in our model because the intrusion rate never varies, we would expect more complexity with a more geometrically and temporally varying intrusion rate. Fig. 12b shows the corresponding drop in temperature of the bulk erupted melts as basaltic eruptions are stopped during the caldera cycle, even as the rhyolites themselves increase in temperature from <800 °C to over 900 °C.

6. Discussion

Our coupled magmatic-thermomechanical models provide valuable insight into the possible origins of the compositional trends that we observe in Yellowstone hot spot track rhyolites and provide an important new test for existing models. We investigate multiple possible methods of generating low-$\delta^{18}O$ rhyolites, and provide a possible explanation for the existence of isotopically ancient rhyolites early in the eruptive cycle of some caldera centers. We also make some preliminary observations of the types of chemical and thermal trends that occur in erupted magmas, anticipating possible further research. First, however, we reexamine some of the controls on the total volume of melt which erupts at all.

6.1. Structural controls on cumulative erupted volume

In both the I2VIS and Heat2D models, we observe that models with smaller and more frequent eruptions yield significantly greater total eruptive volume than a few extremely large eruptions (Figs. 6, 7)

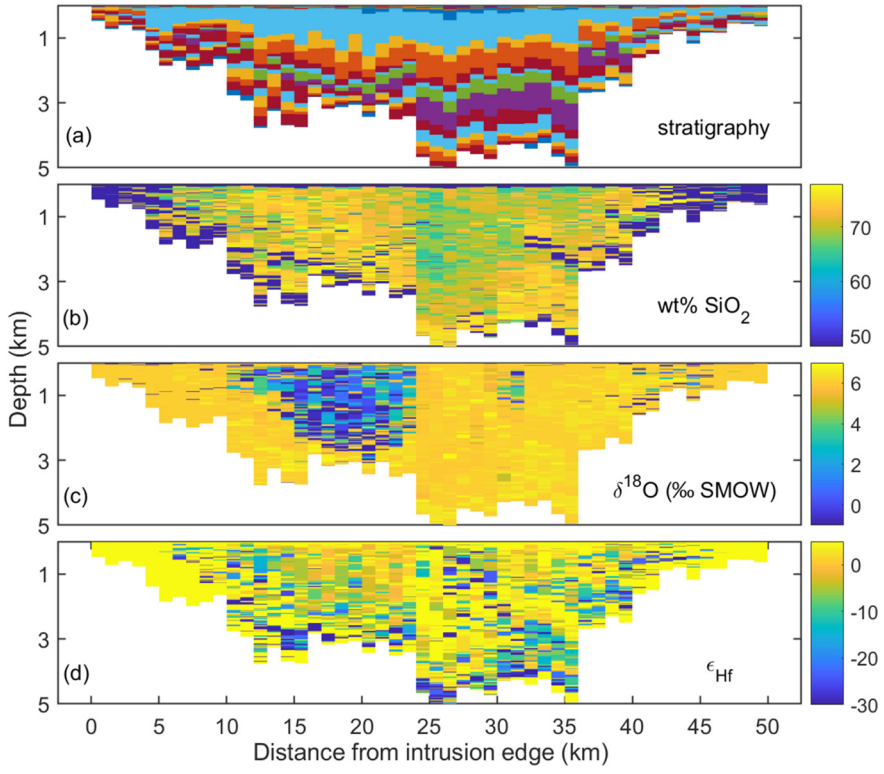

Fig. 11. Intracaldera isotopic stratigraphy from the I2VIS model depicted in Fig. 2. (a) Intracaldera stratigraphy, with each eruption assigned its own color. Note the very large eruption late in the sequence with up to 1.5 km-thick deposits. (b) SiO_2 content of erupted material, showing that basalts erupt at the start of the system's activity (base of the sequence) and at the margins of the caldera system. The center of the system is host to the hottest magmas, which are slightly less silicic, though basalts are still essentially absent. (c) O isotope stratigraphy shows that the production of low-$\delta^{18}O$ magmas is highly localized in the crust, in real systems these magmas would then likely mix over a greater horizonal area, unlike here where magmas only erupt purely vertically. (d) Hf isotope stratigraphy shows a trend towards more mantle-like values (higher ε_{Hf}) in younger units higher in the sequence. The strong spatial diversity of $\delta^{18}O$ and ε_{Hf} at each level is consistent with the zircon diversity seen in the rock record (Bindeman and Simakin, 2014; Colón et al., 2018b).

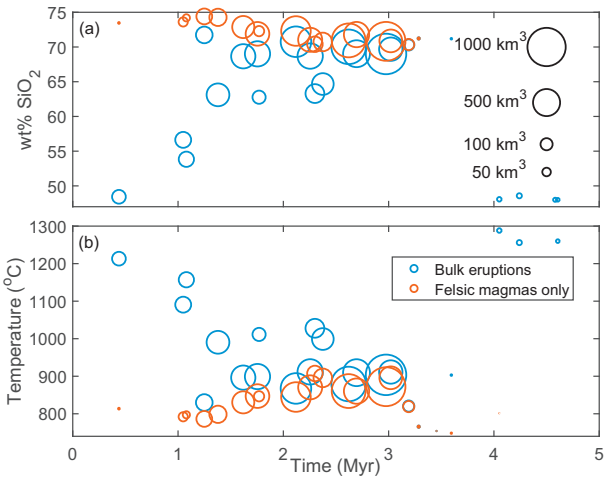

Fig. 12. SiO_2 content (a) and temperature (b) of erupted magmas over time for the model depicted in Figs. 2–5 and 10–11. For the 3 Myr lifetime of the system, bulk magma SiO_2 contents increase while temperatures decrease as less basaltic melt erupts, as it is trapped by the silicic magma body. Considering only felsic melts, we note opposite trends as erupted rhyolites become less silicic and hotter with time. Finally, the system eventually returns to erupting almost exclusively hot basalt in the post-caldera stage of the system's evolution.

separated by long repose intervals, which are controlled presumably by structural properties of the uppermost crust beyond the purview of our models (e.g. Gregg et al., 2015). It appears that at least two separate effects are at play here. For the Heat2D results, we recall that only crustal melts are erupted, and that all mafic melts and their fractionates remain in the crust. In this case, the anticorrelation between eruption repose time and total erupted volume may be explained by thinking in terms of the most efficient way to produce and erupt melt. As soon as any crust is melted, additional heat to bring it above its melting temperature can be considered "wasted" heat that could be instead devoted to melting more crust. To avoid this, erupting crustal melts to the surface shortly after they form allows new cold crust to come into contact with the hot mafic intrusions. Doing this more often, as occurs in models with shorter eruption repose times, allows a greater total volume of crust to melt. By this interpretation, the largest total eruptive volumes (aka continuous eruptions) seen in Fig. 7c–d may represent a limit to the amount of crust that can be melted by a 15 km sill complex of basalt intruded to 7 km depth over 2 Myr. In Fig. 7a, we note that there is much less mafic melt in the crust at any time in the scenario with more eruptions, even though it cannot erupt, suggesting that the enthalpy of the mafic intrusion is being carried away by the many eruptions.

This idea is not entirely adequate to explain the same phenomenon observed in our thermomechanical models (Fig. 6), where basaltic melts and their fractionates can also erupt. We actually find that there is a negative correlation between the repose time and the total amount of melt produced in the crust, including material that never erupts (Fig. 6b). This suggests that the cooling effect of more eruptions slightly inhibits melt production in the crust. However, there is a stronger correlation between the total amount of melt that erupts and the number of eruptions. This apparent contradiction is resolved in Fig. 6c, which shows that more eruptions are associated with a much higher volcanic-plutonic ratio. This means that despite the somewhat lessened amount of melt which is produced when there are more eruptions, the system much more efficiently erupts that material to the surface, more than canceling out the former effect. Fig. 6d clearly demonstrates that the increased volcanic-plutonic ratio which occurs shorter eruption repose times is the driver of variations in the total erupted volume. The very high r^2 value of 0.94 also suggests that other variations in eruptive volume that occur in models with similar eruption repose times can also be best described not in terms of total melt production but in terms of how the geometry of the system affects the volcanic-plutonic ratio. An interesting additional conclusion we can make is that this modeling suggests that small systems that erupt frequently are more likely to leave most of their felsic melts on the surface in the form of volcanic deposits, while large systems that erupt infrequently extract melt less efficiently, thermodynamically speaking, when they do erupt and are more likely to leave behind large plutons.

Cooling rates also provide the key explanation for why the wider intrusions shown in Figs. 8–9 are so much less magmatically productive, despite the total enthalpy being delivered to the crust per kilometer of horizontal model space being the same. At the very shallow depths where melting primarily takes place in these models, cooling from the surface is a critical control on the amount of rhyolite melt that can form. As such, the increased crustal thickening rate for the narrow models is much more effective at generating rhyolite than the longer intrusion duration of the wider models. Despite this, many of the eruptive centers along the Yellowstone hot spot track produced several 1000's of km^3 of rhyolite over durations and areas similar to that seen in Fig. 8d, especially in the central Snake River Plain. This suggests that to have significant rhyolite volumes erupted over 4 Myr or more (e.g. Drew et al., 2013; Bonnichsen et al., 2008; Knott et al., 2016), basalt intrusion rates were not the long, slow and steady rates used to make the Fig. 9 models, but were likely either punctuated by brief periods of much more intense intrusion and heating or where characterized by multiple separate focused areas of intrusions. Further understanding of the precise geometry of the intrusive zones that fuel super-eruptive caldera centers will almost certainly be an important topic for future modeling, particularly 3D modeling and models what are able to accommodate nonvertical diking in the crust.

6.2. The origin of isotopically ancient rhyolites

The Yellowstone hot spot track is characterized by several extremely low-ε_{Hf} eruptions which require the melting of large volumes of Precambrian crust, most notably the Johnstones Camp Rhyolite in the central Snake River Plain (Colón et al., 2015a), the Arbon Valley Tuff at the Picabo center (Drew et al., 2013, 2016), and Huckleberry Ridge Tuff Member C at Yellowstone (Wotzlaw et al., 2015). These eruptions all occurred within 1.0 Myr of the start of activity at their respective volcanic centers (Fig. 1; Colón et al., 2018b). In our models, we successfully replicate a trend of initially low-ε_{Hf} eruptions at the start of the cycle of activity which eventually give way to more mantle-like eruptions (Fig. 10a). The crustal melts which fuel these low-ε_{Hf} eruptions are nearly entirely derived from the melting of the 2 km-thick fertile layer (orange, Fig. 2) which forms a boundary between the upper crust and lower crust, but which is isotopically ancient. If we remove this layer and replace it with more refractory "normal" lower crust (gray, Fig. 2), or with more upper crust, this effect vanishes, and all erupted rhyolites are relatively radiogenic with respect to Hf isotopes (see the Appendix). We therefore propose that the necessary precondition for producing an initial Precambrian crust-like eruption is a relatively fertile piece of Precambrian crust which melts before the bulk of the upper crust, largely as a function of its greater depth. This is confirmed in Fig. 5, in which isotopically ancient uppermost lower crust begins melting about 1 Myr before the upper crust. Such rocks should be relatively rare, as the long history of Cenozoic volcanism and intrusive magmatism in the region (Chadwick, 1985; Gaschnig et al., 2010) should have provided many opportunities for such crust to be heated, melted, and stripped of its fertile components. This is likely the reason that very low-ε_{Hf} magmas are not more common along the Yellowstone hot spot track, and they appear to be absent among rocks described so far from the Heise and Twin Falls centers (Fig. 1, Bindeman and Simakin, 2014; Colón et al., 2018b).

6.3. Caldera collapse-driven crustal melting and the production of low-$\delta^{18}O$ magmas

The fact that voluminous low-ε_{Hf} magmas only occur early in the evolution of Yellowstone volcanic centers, and the fact that low-$\delta^{18}O$ magmas become more common with time suggests that the mix of crustal rocks that melt to produce erupted rhyolites changes with time, which we confirm in our models (Fig. 5). Previous workers have suggested that low-$\delta^{18}O$ rhyolites were formed by the burial and remelting of the earliest rocks in the eruptive cycle, which were hydrothermally altered shortly after emplacement by a hydrothermal system similar to the one at Yellowstone today (Watts et al., 2011; Drew et al., 2013; Bindeman and Simakin, 2014; Colón et al., 2018b). We test this model with both the Heat2D and I2VIS codes, and find that, in our models, that the first erupted rhyolites are never buried deeply enough beneath the products of later eruptions to be remelted, which likely rules out the direct remelting of large volumes of older volcanic rocks, but not of their deeper subvolcanic intrusive equivalents, which may also include such features as significantly low-$\delta^{18}O$ hydrothermally-derived porphyry deposits.

We do, however, find a clear potential role for caldera collapse in generating these isotopic trends. As is demonstrated in the illustration of a Heat2D model in Fig. 13, magma evacuation and caldera collapse above a mid-crustal basaltic sill complex with stable depth results in progressively shallower crust melting and erupting at the surface. The resulting 3–4 km-thick nested caldera complex will thus have the same isotopic stratigraphy as the 3–4 km of crustal material which lies above the initial depth of the growing sill complex. If the top of the mid-crustal sill lies just below the boundary between low-ε_{Hf}, but fertile, lower crust and more isotopically primitive upper crust, this transition will also manifest in the overlying eruptive stratigraphy. Similarly, if the upper crust becomes more depleted in ^{18}O with decreasing depth, the later eruptions, which result from the melting of progressively more shallow crust, should have a more low-$\delta^{18}O$ composition as well.

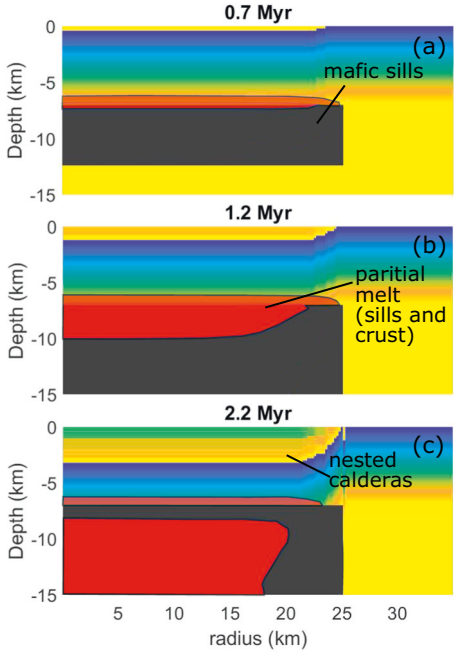

Fig. 13. Evolution of a Heat2D model where 15 km of basalt intrudes at a depth of 7 km over a duration of 2.0 Myr. Four eruptions occur at intervals of 0.5 Myr. Black areas are the growing sill complex, and red areas are areas of partial melt, in both the sill and the surrounding crust. The color scheme in the surrounding crust simply corresponds to depth, but could be thought of as an analog for any isotopic tracer such as O or Hf isotopes. A ~3 km-deep nested caldera complex forms, with the earliest eruptions having the "yellow" composition characteristic of the 7 km depth where melting begins, followed by eruptions with the progressively shallower crust that is advected down towards the heat source of the sill by repeated magma evacuation and caldera collapse. (For interpretation of the references to color in this figure legend, the reader is referred to the web version of this article.)

We see similar patterns when examining the I2VIS models. In Figs. 11c–d, we show the isotopic stratigraphy resulting from the I2VIS model seen in Figs. 2–4, specifically recreating the trends seen in Fig. 10. We see the progression towards progressively more upper crustal-like ε_{Hf} and $\delta^{18}O$ values as we move higher in the eruptive stratigraphy, though this is obscured by the horizontal variations in what is melting. Comparing this view to Fig. 13, we see that the story of progressively shallower depths of crustal melting is less clear-cut than in the Heat2D models, but the Hf isotope stratigraphy seen in Figs. 10–11 again strongly suggests that crust at deeper levels melts first (orange material in Fig. 2). Adding further credence to the importance of caldera collapse to producing low-$\delta^{18}O$ magmas, we note that the I2VIS model with short repose times, much greater cumulative eruptive volume (Fig. 9), and therefore a greater total caldera subsidence depth, shows smoother trends towards low$\delta^{18}O$ and higher-ε_{Hf} eruptions over time than the standard model with less total eruptive volume and hybridization of melts. Finally, we note that we cannot entirely rule out the remelting of buried intracaldera rocks, as caldera collapse structures in nature can be much more complex than the structures we see in our models, and may produce locally very thick sections of intracaldera material. These may be produced by concentrating upper crustal melts into less laterally-extensive structures through horizontal melt migration to a more roughly spherical melt body, possibly driven by an incipient magma body's effect on local dikes (e.g. Karlstrom et al., 2009). The existence of super-thick intracaldera tuffs from single eruptions in the geologic record is also confirmed by some of the tilted and dissected sections seen in the older Basin and Range province south of the Yellowstone hot spot track, most notably in the ~4 km thick Caetano Tuff (John et al., 2008). Again, this may be a fruitful future area for 3D and higher-resolution modeling with more a sophisticated treatment of nonvertical melt transport.

6.4. Origin of low-$\delta^{18}O$ magmas by burial of crust under intrusions

We here describe an additional possible explanation for the origin of low-$\delta^{18}O$ magmas by examining the distribution of oxygen isotopes in the I2VIS models. In Fig. 14, we map the $\delta^{18}O$ values of the upper and mid crust in the standard model seen in Fig. 2. Recall that the I2VIS models use a very simplified scheme for hydrothermal alteration, where crust is "reset" to low-$\delta^{18}O$ values if it is weakened below an effective viscosity of 10^{22} Pa·s, has a temperature between 100 and 300 °C, and exists in a geothermal gradient of >40 °C/km. This results in the rapid development of a zone of low-$\delta^{18}O$ crust above the mafic sill complex which is mature as early as 0.25 Myr after the start of intrusions into the crust. As this layer of low-$\delta^{18}O$ material is heated from below, it can melt and erupt at the surface, as in Fig. 13. However, we also observe that some of this initial low-$\delta^{18}O$ crustal layer is overplated by further intrusions of basalt, and gradually advected down to depths of as great as 20 km by continued burial by intrusions of basalt over the next 2 Myr. There, it is heated to temperatures approaching the liquidus temperature of upper crust (Figs. 2–3), where it melts and releases low-$\delta^{18}O$ material to the surface as eruptions. Tellingly, comparing Figs. 11 and 14 shows that the two areas of low-$\delta^{18}O$ material in the lower crust correspond to two equivalent areas in the overlying caldera with more low-$\delta^{18}O$ material, suggesting that this overplating and deep burial may be the most important single mechanism for producing voluminous low-$\delta^{18}O$ rhyolites in the Yellowstone hot spot track and elsewhere. In particular, the hot and voluminous low-$\delta^{18}O$ magmas in the central Snake River Plain may have been partially produced in this way, especially if the crust there was low-$\delta^{18}O$ to begin with (Boroughs et al., 2012; Colón et al., 2015a), making the overplating and burial of initially low-$\delta^{18}O$ crust a trivial matter.

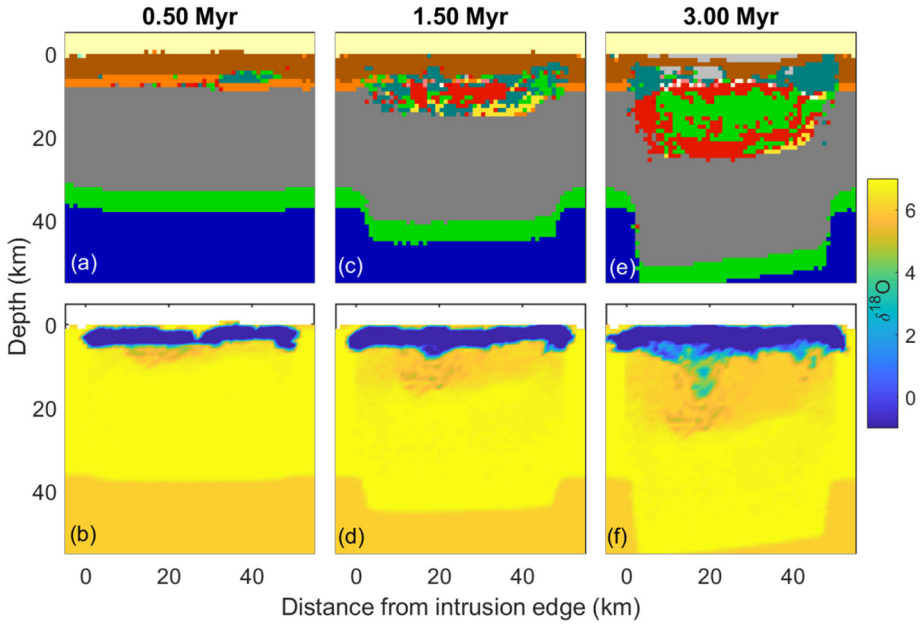

Fig. 14. Map of oxygen isotopes in the upper and mid crust in our standard I2VIS model. We note that a robust layer of low-$\delta^{18}O$ crust manifests above the incipient intrusions by as early as 0.5 Myr after intrusions begins (a–b) but cannot advance to greater depths because they are too hot for hydrothermal circulation to occur. Instead, we observe that the developing mafic sill complex "bites off" part of the shallow low-$\delta^{18}O$ layer, and subsequent repeated overplating by basalt advects that material with a bulk $\delta^{18}O$ value as low as +2‰ down to depths of as great as 20 km (c–f), where it is heated to temperatures of over 900 °C, melting it extensively.

The eventual depletion of this material may cause a temporary "recovery" towards normal $\delta^{18}O$ values in the erupted material (Figs. 10–11), as has been documented in both the central Snake River Plain and in the post-caldera lavas at Yellowstone (Watts et al., 2012; Loewen and Bindeman, 2015; Colón et al., 2015a). Finally, we note that the part of the caldera complex in Fig. 11 which is the source of low-$\delta^{18}O$ magmas is less productive (less thick) than the part which makes more mantle-like magmas, suggesting that there is a significant thermal penalty to melting significant quantities of upper crust rather than simply fractionating large amounts of basalt, resulting in somewhat lower melt production overall (making the huge volumes of low-$\delta^{18}O$ magmas erupted at the central Snake River Plain even more impressive).

6.5. Combining the Hf and O isotopic records

In Fig. 15, we show the bulk eruption Hf and O isotope compositions from our standard (Fig. 2) I2VIS model and four additional runs where the only difference was the exact timing of the eruptions, allowing for a greater sampling of the potential variability of melt compositions. Unlike in Fig. 10, we plot circles that reflect just the weighted average compositions of markers which are at least 70% silica, as more mafic markers are assumed to likely be silica undersaturated. This is why there is a greater range in isotopic values in Fig. 15 than in Fig. 10, despite being sourced from the same model, and it greatly improves the match with the zircon data, which is the same dataset from the Picabo and Yellowstone centers (Fig. 1) seen in Fig. 10. This dataset has a characteristic L-shape, requiring three component mixing (Colón et al., 2018b), but with a distinct lack of mixing between the low-ε_{Hf} and low-$\delta^{18}O$ end-members. Our models recreate this trend by having melting of isotopically ancient lower crust and hydrothermally altered upper crust occur at different times and places in the model, suggesting that our assumptions about magma transport and the structure of the crust are broadly correct. Other crustal geometries that, for example, lack a fertile uppermost lower crust or have thicker upper crust produce melt compositions which cover part but not necessarily all of the data field in Fig. 15. Critically, only models like our standard model in Fig. 2 with ~5 km of upper crust underlain by fertile but isotopically ancient lower crust produce the initial super-low ε_{Hf} magmas seen in Fig. 10. This places an important constraint on the thickness of the fertile upper crust in the Yellowstone region, one which is broadly supported by geophysical observations (Peng and Humphreys, 1998) and by nearby exposures in places like the Teton Range (e.g. Roberts and Douglas, 1993).

7. Conclusions

We use a modification of the I2VIS code of Gerya and Yuen (2003) and Colón et al. (2018a) and the Heat2D code of Annen (2009) and

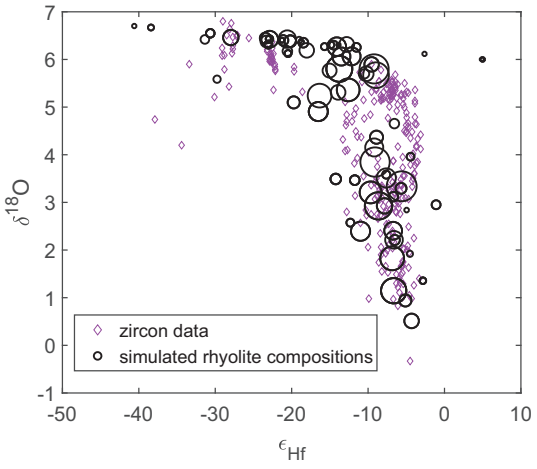

Fig. 15. Plot of bulk eruption $\delta^{18}O$ and ε_{Hf} values from two I2VIS model runs compared to the actual isotopic record from zircon from the Yellowstone and Picabo centers of the hotspot track (Colón et al., 2018b). To better match zircon values which may occur in eruptions, only erupted markers with at least 70% SiO_2 were used to calculate isotopic values, as we assume more mafic melts are zircon undersaturated. The black circles represent eruptions from five individual models run with the same initial conditions and model physics as the model in Fig. 2, to achieve more through coverage of the data field. We note an excellent match between simulated and real isotopic values. Circle sizes weight the relative size of eruptions, but do not correspond to particular values because of the exclusion of the more mafic melts from each value.

Annen et al. (2008) to investigate the controls on the compositions of erupted rhyolites at the nested caldera complexes of the Yellowstone hot spot track. Building on the work of Colón et al. (2018a), we model the intrusion of basalt in a 50 km-wide area for 3 Myr, resulting in a thickening of the crust by approximately 20 km. Intruding basalts primarily accumulate in a large mid-crustal sill complex at depths of 8–24 km, resulting in the extensive reworking of the crustal column and the eruption of as much as 5000 km^3 of rhyolite. We make several new observations about the chemical and isotopic evolution of the erupted rhyolites. (1) We find that making volcanic eruptions more frequent increases the total volume of melt which erupts through increasing the efficiency of the delivery of heat to the crust, and through increasing the volcanic-plutonic ratio. (2) The modeled evolution of the chemical and isotopic compositions of the erupted rhyolites replicates natural trends towards less isotopically ancient Hf isotopes over time. Later erupted magmas are also hotter and less silica-rich. We interpret this as reflecting a regime in which early eruptions are dominated by melts of the uppermost lower crust, which we assume is isotopically ancient but fertile, and in which later eruptions are dominated by melts of the upper crust and fractionates of the growing basaltic sill complex. In all of these ways, the erupted rhyolites gradually more closely resemble the chemical and isotopic composition of the basalts from the mantle that enable their eruption, reflecting the "mantleization" of and the mid crust during continental hot spot volcanism. (3) The sole exception to this trend is in the $\delta^{18}O$ values of the erupted rhyolites, which become progressively lower than normal mantle-like values over time. We test models for the origin of this trend, which is well-documented in the actual volcanic products of the hot spot track (Bindeman and Simakin, 2014; Colón et al., 2018b). Heat balance modeling suggests that remelting of already-erupted caldera-filling ignimbrites may be quite minor in the real world but melting of subcaldera hydrothermally altered crust, especially crust which is initially slightly shallower than the depth of melting and dropped into the sill complex by caldera collapse is a viable possibility. (4), We also find and describe an additional previously unappreciated means of generating low-$\delta^{18}O$ rhyolites through advecting shallow crust which is altered to low $\delta^{18}O$ values and then buried to depths of 20 km or more by repeated overplating of basalt, where it can extensively melt. (5) The good match between our isotopic (O, Hf), chemical (SiO_2), and temperature trends with those of the actual Yellowstone hotspot track suggests the crustal structure we used (Fig. 2), which we constrained from both geophysical imaging and the fact that very different structures fail to reproduce these trends is evidence that this structure is likely a fairly good match with the actual crustal stratigraphy in the region. Finally (6), we note that at Yellowstone, the completed evolution towards magmas with mantle-like radiogenic isotopes and low $\delta^{18}O$ values, the significant (~5000 km^3) cumulative erupted volume, and the presence of an amagmatic gap at depths of ~20 km (possibly indicating a thick and mature cumulated pile, as in Figs. 2d–e and 3c–d) indicate that this volcanic system may be relatively close to the end of its life cycle. It is therefore reasonable to expect the next caldera-forming eruption there will occur in less thoroughly processed crust to the northeast of the present caldera, perhaps near Sour Creek Dome, and likely with low ε_{Hf} and normal-$\delta^{18}O$ magmas.

Acknowledgments

We would like to thank Paul Wallace and Gene Humphreys at the University of Oregon for feedback on this manuscript. We also thank Catherine Annen for sharing the Heat2D code and Oleg Melnik for advice on melt extraction methodology. This research was supported by grants NSF EAR 1822977 and CAREER-844772, as well as funding from the University of Oregon Department of Earth Sciences. Finally, we thank two anonymous reviewers for their valuable feedback.

Appendices: Detailed Methods and Supplementary Data

Supplementary data to this article can be found online at https://doi.org/10.1016/j.jvolgeores.2018.12.003.

References

Allan, A.S.R., Wilson, C.J.N., Millet, M.A., Wysoczanski, R.J., 2012. The invisible hand: Tectonic triggering and modulation of a rhyolitic supereruption. Geology 40, 563–566. https://doi.org/10.1130/G32969.1.

Almeev, R.R., Bolte, T., Nash, B.P., Holtz, F., Erdmann, M., Cathey, H.E., 2012. High-temperature, low-H 2O silicic magmas of the yellowstone hotspot: an experimental study of rhyolite from the Bruneau-Jarbidge eruptive center, Central Snake River Plain, USA. J. Petrol. 53, 1837–1866. https://doi.org/10.1093/petrology/egs035.

Annen, C., 2009. From plutons to magma chambers: thermal constraints on the accumulation of eruptible silicic magma in the upper crust. Earth Planet. Sci. Lett. 284, 409–416. https://doi.org/10.1016/j.epsl.2009.05.006.

Annen, C., Sparks, R.S.J., 2002. Effects of repetitive emplacement of basaltic intrusions on thermal evolution and melt generation in the crust. Earth Planet. Sci. Lett. 203, 937–955. https://doi.org/10.1016/S0012-821X(02)00929-9.

Annen, C., Blundy, J.D., Sparks, R.S.J., 2006. The genesis of intermediate and silicic magmas in deep crustal hot zones. J. Petrol. 47, 505–539. https://doi.org/10.1093/petrology/egi084.

Annen, C., Blundy, J.D., Leuthold, J., Sparks, R.S.J., 2015. Construction and evolution of igneous bodies: towards an integrated perspective of crustal magmatism. Lithos https://doi.org/10.1016/j.lithos.2015.05.008.

Barton, K.E., Howell, D.G., Vigil, J.F., 2003. The North American tapestry of time and terrain, scale 1:8000000. USGS Geologic Investigations Series I 2781.

Bindeman, I., 2008. Oxygen isotopes in mantle and crustal magmas as revealed by single crystal analysis. Rev. Mineral. Geochem. 69, 445–478. https://doi.org/10.2138/rmg.2008.69.12.

Bindeman, I.N., Simakin, A.G., 2014. Rhyolites-Hard to produce, but easy to recycle and sequester: Integrating microgeochemical observations and numerical models. Geosphere 10, 930–957. https://doi.org/10.1130/GES00969.1.

Bindeman, I.N., Valley, J.W., 2001. Low-delta O-18 rhyolites from Yellowstone: magmatic evolution based on analyses of zircons and individual phenocrysts. J. Petrol. 42, 1491–1517. https://doi.org/10.1093/petrology/42.8.1491.

Blum, T.B., Kitajima, K., Nakashima, D., Strickland, A., Spicuzza, M.J., Valley, J.W., 2016. Oxygen isotope evolution of the Lake Owyhee volcanic field, Oregon, and implications for the low-?18O magmatism of the Snake River Plain? Yellowstone hotspot and other low-?18O large igneous provinces. Contrib. Mineral. Petrol. 171, 92. https://doi.org/10.1007/s00410-016-1297-x.

Bonnichsen, B., Leeman, W.P., Honjo, N., McIntosh, W.C., Godchaux, M.M., 2008. Miocene silicic volcanism in southwestern Idaho: geochronology, geochemistry, and evolution of the central Snake River Plain. Bull. Volcanol. 70, 315–342. https://doi.org/10.1007/s00445-007-0141-6.

Boroughs, S., Wolff, J.A., Ellis, B.S., Bonnichsen, B., Larson, P.B., 2012. Evaluation of models for the origin of Miocene low-?? 18O rhyolites of the Yellowstone/Columbia River Large Igneous Province. Earth Planet. Sci. Lett. 313–314, 45–55. https://doi.org/10.1016/j.epsl.2011.10.039.

Branney, M.J., Bonnichsen, B., Andrews, G.D.M., Ellis, B., Barry, T.L., McCurry, M., 2008. "Snake River (SR)-type" volcanism at the Yellowstone hotspot track: distinctive products from unusual, high-temperature silicic super-eruptions. Bull. Volcanol. 70, 293–314. https://doi.org/10.1007/s00445-007-0140-7.

Burov, E., Gerya, T.V., 2014. Asymmetric three-dimensional topography over mantle plumes. Nature 513, 85–89. https://doi.org/10.1038/nature13703.

Burov, E., Guillou-Frottier, L., 2005. The plume head-continental lithosphere interaction using a tectonically realistic formulation for the lithosphere. Geophys. J. Int. 161, 469–490. https://doi.org/10.1111/j.1365-246X.2005.02588.x.

Burov, E., Guillou-Frottier, L., D'Acremont, E., Le Pourhiet, L., Cloetingh, S., 2007. Plume head-lithosphere interactions near intra-continental plate boundaries. Tectonophysics 434, 15–38. https://doi.org/10.1016/j.tecto.2007.01.002.

Cao, W., Kaus, B.J.P., Paterson, S., 2016. Intrusion of granitic magma into the continental crust facilitated by magma pulsing and dike-diapir interactions: numerical simulations. Tectonics 35, 1575–1594. https://doi.org/10.1002/2015TC004076.

Cathey, H.E., Nash, B.P., 2009. Pyroxene thermometry of rhyolite lavas of the Bruneau-Jarbidge eruptive center, Central Snake River Plain. J. Volcanol. Geotherm. Res. 188, 173–185. https://doi.org/10.1016/j.jvolgeores.2009.05.024.

Chadwick, R.A., 1985. Overview of Cenozoic Volcanism in the West-Central United States. 359–381.

Christiansen, R.L., 2001. The Quaternary and Pliocene Yellowstone Plateau volcanic field of Wyoming, Idaho, and Montana. U. S. Geol. Surv. Prof. Pap. 729–G, 145.

Christiansen, E.H., McCurry, M., 2008. Contrasting origins of Cenozoic silicic volcanic rocks from the western Cordillera of the United States. Bull. Volcanol. 70, 251–267. https://doi.org/10.1007/s00445-007-0138-1.

Colón, D.P., Bindeman, I.N., Ellis, B.S., Schmitt, A.K., Fisher, C.M., 2015a. Hydrothermal alteration and melting of the crust during the Columbia River Basalt-Snake River Plain transition and the origin of low-$\delta^{18}O$ rhyolites of the central Snake River Plain. Lithos 224–225, 310–323. https://doi.org/10.1016/j.lithos.2015.02.022.

Colón, D.P., Bindeman, I.N., Stern, R.A., Fisher, C.M., 2015b. Isotopically diverse rhyolites coeval with the Columbia River Flood Basalts: evidence for mantle plume interaction with the continental crust. Terra Nova 27, 270–276. https://doi.org/10.1111/ter.12156.

Colón, D.P., Bindeman, I.N., Gerya, T.V., 2018a. Thermomechanical modeling of the formation of a multilevel, crustal-scale magmatic system by the Yellowstone plume. Geophys. Res. Lett. https://doi.org/10.1029/2018GL077090.

Colón, D.P., Bindeman, I.N., Wotzlaw, J.-F., Christiansen, E.H., Stern, R.A., 2018b. Origins and evolution of rhyolitic magmas in the central Snake River Plain: insights from coupled high-precision geochronology, oxygen isotope, and hafnium isotope analyses of zircon. Contrib. Mineral. Petrol. 173, 11. https://doi.org/10.1007/s00410-017-1437-y.

Doe, B.R., Leeman, W.P., Christiansen, R.L., Hedge, C.E., 1982. Lead and strontium isotopes and related trace elements as genetic tracers in the Upper Cenozoic rhyolite-basalt association of the Yellowstone Plateau Volcanic Field. J. Geophys. Res. 87, 4785–4806. https://doi.org/10.1029/JB087iB06p04785.

Drew, D.L., Bindeman, I.N., Watts, K.E., Schmitt, A.K., Fu, B., McCurry, M., 2013. Crustal-scale recycling in caldera complexes and rift zones along the Yellowstone hotspot track: O and Hf isotopic evidence in diverse zircons from voluminous rhyolites of the Picabo volcanic field, Idaho. Earth Planet. Sci. Lett. 381, 63–77. https://doi.org/10.1016/j.epsl.2013.08.007.

Drew, D.L., Bindeman, I.N., Loewen, M.W., Wallace, P.J., 2016. Initiation of large-volume silicic centers in the Yellowstone hotspot track: insights from H2O- and F-rich quartz-hosted rhyolitic melt inclusions in the Arbon Valley Tuff of the Snake River Plain. Contrib. Mineral. Petrol. 171, 1–20. https://doi.org/10.1007/s00410-015-1210-z.

Dufek, J., Bergantz, G.W., 2005. Lower crustal magma genesis and preservation: a stochastic framework for the evaluation of basalt-crust interaction. J. Petrol. 46, 2167–2195. https://doi.org/10.1093/petrology/egi049.

Ellis, B.S., Wolff, J.A., Boroughs, S., Mark, D.F., Starkel, W.A., Bonnichsen, B., 2013. Rhyolitic volcanism of the central Snake River Plain: a review. Bull. Volcanol. 75, 1–19. https://doi.org/10.1007/s00445-013-0745-y.

Farrell, J., Smith, R.B., Husen, S., Diehl, T., 2014. Tomography from 26 years of seismicity revealing that the spatial extent of the Yellowstone crustal magma reservoir extends well beyond the Yellowstone caldera. Geophys. Res. Lett. 41, 3068–3073. https://doi.org/10.1002/2014GL059588.

Fisher, C.M., Vervoort, J.D., Hanchar, J.M., 2014. Guidelines for reporting zircon Hf isotopic data by LA-MC-ICPMS and potential pitfalls in the interpretation of these data. Chem. Geol. 363, 125–133. https://doi.org/10.1016/j.chemgeo.2013.10.019.

Gaschnig, R.M., Vervoort, J.D., Lewis, R.S., McClelland, W.C., 2010. Migrating magmatism in the northern US Cordillera: in situ U-Pb geochronology of the Idaho batholith. Contrib. Mineral. Petrol. 159, 863–883. https://doi.org/10.1007/s00410-009-0459-5.

Gerya, T., 2010. Introduction to Numerical Geodynamic Modelling. Cambridge University Press https://doi.org/10.1017/CBO9780511809101.

Gerya, T.V., Burg, J.P., 2007. Intrusion of ultramafic magmatic bodies into the continental crust: numerical simulation. Phys. Earth Planet. Inter. 160, 124–142. https://doi.org/10.1016/j.pepi.2006.10.004.

Gerya, T.V., Yuen, D.A., 2003. Characteristics-based marker-in-cell method with conservative finite-differences schemes for modeling geological flows with strongly variable transport properties. Phys. Earth Planet. Inter. 140, 293–318. https://doi.org/10.1016/j.pepi.2003.09.006.

Gerya, T.V., Stern, R.J., Baes, M., Sobolev, S.V., Whattam, S.A., 2015. Plate tectonics on the Earth triggered by plume-induced subduction initiation. Nature 527, 221–225. https://doi.org/10.1038/nature15752.

Gottardi, R., Kao, P.H., Saar, M.O., Teyssier, C., 2013. Effects of permeability fields on fluid, heat, and oxygen isotope transport in extensional detachment systems. Geochem. Geophys. Geosyst. 14, 1493–1522. https://doi.org/10.1002/ggge.20100.

Gregg, P.M., Grosfils, E.B., de Silva, S.L., 2015. Catastrophic caldera-forming eruptions II: the subordinate role of magma buoyancy as an eruption trigger. J. Volcanol. Geotherm. Res. 305, 100–113. https://doi.org/10.1016/j.jvolgeores.2015.09.022.

Hess, P.C., 1989. Origins of Igneous Rocks. Harvard University Press.

Hildreth, W., Christiansen, R.L., O'Neil, J.R., 1984. Catastrophic isotopic modification of rhyolitic magma at times of caldera subsidence, Yellowstone Plateau Volcanic Field. J. Geophys. Res. 89, 8339–8369. https://doi.org/10.1029/JB089iB10p08339.

Hildreth, W., Halliday, A.N., Christiansen, R.L., 1991. Isotopic and chemical evidence concerning the genesis and contamination of basaltic and rhyolitic magmas beneath the Yellowstone Plateau Volcanic Field. J. Petrol. 32, 63–138.

Honjo, N., Bonnichsen, B., Leeman, W.P., Stormer, J.C., 1992. Mineralogy and geothermometry of high-temperature rhyolites from the central and western Snake River Plain. Bull. Volcanol. 54, 220–237. https://doi.org/10.1007/BF00278390.

Hopper, E., Ford, H.A., Fischer, K.M., Lekic, V., Fouch, M.J., 2014. The lithosphere-asthenosphere boundary and the tectonic and magmatic history of the northwestern United States. Earth Planet. Sci. Lett. 402, 69–81. https://doi.org/10.1016/j.epsl.2013.12.016.

Huang, H.-H., Lin, F.-C., Schmandt, B., Farrell, J., Smith, R.B., Tsai, V.C., 2015. The Yellowstone magmatic system from the mantle plume to the upper crust. Science 348, 773–776. https://doi.org/10.1126/science.aaa5648 (80-.).

Huppert, H.E., Sparks, R.S.J., 1988. The generation of granitic magmas by intrusion of basalt into continental crust. J. Petrol. 29, 599–624. https://doi.org/10.1093/petrology/29.3.599.

Jellinek, A.M., DePaolo, D.J., 2003. A model for the origin of large silicic magma chambers: precursors of caldera-forming eruptions. Bull. Volcanol. 65, 363–381. https://doi.org/10.1007/s00445-003-0277-y.

Johannes, W., 1985. The significance of experimental studies for the formation of migmatites. Migmatites. Springer US, Boston, MA, pp. 36–85 https://doi.org/10.1007/978-1-4613-2347-1_2.

John, D.A., Henry, C.D., Colgan, J.P., 2008. Magmatic and tectonic evolution of the Caetano caldera, north-central Nevada: a tilted, mid-Tertiary eruptive center and source of the Caetano Tuff. Geosphere 4, 75–106. https://doi.org/10.1130/GES00116.1.

Karakas, O., Degruyter, W., Bachmann, O., Dufek, J., 2017. Lifetime and size of shallow magma bodies controlled by crustal-scale magmatism. Nat. Geosci. 10, 446–450. https://doi.org/10.1038/NGEO2959.

Karlstrom, L., Dufek, J., Manga, M., 2009. Organization of volcanic plumbing through magmatic lensing by magma chambers and volcanic loads. J. Geophys. Res. Solid Earth 114, B10204. https://doi.org/10.1029/2009JB006339.

Karlstrom, L., Rudolph, M.L., Manga, M., 2012. Caldera size modulated by the yield stress within a crystal-rich magma reservoir. Nat. Geosci. 5, 402–405. https://doi.org/10.1038/ngeo1453.

Kavanagh, J.L., Menand, T., Sparks, R.S.J., 2006. An experimental investigation of sill formation and propagation in layered elastic media. Earth Planet. Sci. Lett. 245, 799–813. https://doi.org/10.1016/j.epsl.2006.03.025.

Keller, T., May, D.A., Kaus, B.J.P., 2013. Numerical modelling of magma dynamics coupled to tectonic deformation of lithosphere and crust. Geophys. J. Int. 195, 1406–1442. https://doi.org/10.1093/gji/ggt306.

Knott, T.R., Branney, M.J., Reichow, M.K., Finn, D.R., Coe, R.S., Storey, M., Barfod, D., McCurry, M., 2016. Mid-Miocene record of large-scale Snake River-type explosive volcanism and associated subsidence on the Yellowstone hotspot track: the Cassia Formation of Idaho, USA. Bull. Geol. Soc. Am. 128, 1121–1146. https://doi.org/10.1130/B31324.1.

Leeman, W.P., Menzies, M.A., Matty, D.J., Embree, G.F., 1985. Strontium, neodymium and lead isotopic compositions of deep crustal xenoliths from the Snake River Plain: evidence for Archean basement. Earth Planet. Sci. Lett. 75, 354–368. https://doi.org/10.1016/0012-821X(85)90179-7.

Loewen, M.W., Bindeman, I.N., 2015. Oxygen isotope and trace element evidence for three-stage petrogenesis of the youngest episode (260–79 ka) of Yellowstone rhyolitic volcanism. Contrib. Mineral. Petrol. 170, 39. https://doi.org/10.1007/s00410-015-1189-5.

Loewen, M.W., Bindeman, I.N., 2016. Oxygen isotope thermometry reveals high magmatic temperatures and short residence times in Yellowstone and other hot-dry rhyolites compared to cold-wet systems. Am. Mineral. 101, 1222–1227. https://doi.org/10.2138/am-2016-5591.

Maccaferri, F., Bonafede, M., Rivalta, E., 2011. A quantitative study of the mechanisms governing dike propagation, dike arrest and sill formation. J. Volcanol. Geotherm. Res. 208, 39–50. https://doi.org/10.1016/j.jvolgeores.2011.09.001.

McCurry, M., Rodgers, D.W., 2009. Volume of mantle-derived magma. J. Volcanol. Geotherm. Res. 188, 1–13. https://doi.org/10.1016/j.jvolgeores.2009.04.001.

McCurry, M., Hayden, K.P., Morse, L.H., Mertzman, S., 2008. Genesis of post-hotspot, A-type rhyolite of the Eastern Snake River Plain volcanic field by extreme fractional crystallization of olivine tholeiite. Bull. Volcanol. 70, 361–383. https://doi.org/10.1007/s00445-007-0143-4.

Morgan, L.A., McIntosh, W.C., 2005. Timing and development of the Heise volcanic field, Snake River Plain, Idaho, western USA. Bull. Geol. Soc. Am. 117, 288–306. https://doi.org/10.1130/B25519.1.

Nash, B.P., Perkins, M.E., Christensen, J.N., Lee, D.C., Halliday, A.N., 2006. The Yellowstone hotspot in space and time: Nd and Hf isotopes in silicic magmas. Earth Planet. Sci. Lett. 247, 143–156. https://doi.org/10.1016/j.epsl.2006.04.030.

Peng, X., Humphreys, E.D., 1998. Crustal velocity structure across the eastern Snake River Plain and the Yellowstone swell. J. Geophys. Res. 103, 7171–7186. https://doi.org/10.1029/97JB03615.

Pierce, K.L., Morgan, L.A., 2009. Is the track of the Yellowstone hotspot driven by a deep mantle plume? Review of volcanism, faulting, and uplift in light of new data. J. Volcanol. Geotherm. Res. 188, 1–25. https://doi.org/10.1016/j.jvolgeores.2009.07.009.

Poli, S., Schmidt, M.W., 2002. Petrology of subducted slabs. Annu. Rev. Earth Planet. Sci. 30, 207–235. https://doi.org/10.1146/annurev.earth.30.091201.140550.

Ramberg, H., 1971. Dynamic models simulating rift valleys and continental drift. Lithos 4, 259–276. https://doi.org/10.1016/0024-4937(71)90006-5.

Ranalli, G., 1995. Rheology of the Earth. 2nd ed. Springer, Netherlands.

Rivera, T.A., Schmitz, M.D., Jicha, B.R., Crowley, J.L., 2016. Zircon petrochronology and 40Ar/39Ar sanidine dates for the mesa falls tuff: crystal-scale records of magmatic evolution and the short lifespan of a large yellowstone magma chamber. J. Petrol. 57, 1677–1704. https://doi.org/10.1093/petrology/egw053.

Rivera, T.A., Darata, R., Lippert, P.C., Jicha, B.R., Schmitz, M.D., 2017. The duration of a Yellowstone super-eruption cycle and implications for the age of the Olduvai subchron. Earth Planet. Sci. Lett. 479, 377–386. https://doi.org/10.1016/j.epsl.2017.08.027.

Roberts, S.V., Douglas, W.B., 1993. Uplift and thermal history of the Teton Range (northwestern Wyoming) defined by apatite fission-track dating. Earth Planet. Sci. Lett. 118, 295–309. https://doi.org/10.1016/0012-821X(93)90174-8.

Schmidt, M.W., Poli, S., 1998. Experimentally based water budgets for dehydrating slabs and consequences for arc magma generation. Earth Planet. Sci. Lett. 163, 361–379. https://doi.org/10.1016/S0012-821X(98)00142-3.

Schubert, M., Driesner, T., Gerya, T.V., Ulmer, P., 2013. Mafic injection as a trigger for felsic magmatism: a numerical study. Geochem. Geophys. Geosyst. 14, 1910–1928. https://doi.org/10.1002/ggge.20124.

Shervais, J.W., Vetter, S.K., Hanan, B.B., 2006. Layered mafic sill complex beneath the eastern Snake River Plain: evidence from cyclic geochemical variations in basalt. Geology 34, 365–368. https://doi.org/10.1130/G22226.1.

Simakin, A.G., Bindeman, I.N., 2012. Remelting in caldera and rift environments and the genesis of hot, "recycled" rhyolites. Earth Planet. Sci. Lett. 337–338, 224–235. https://doi.org/10.1016/j.epsl.2012.04.011.

Sobolev, S.V., Sobolev, A.V., Kuzmin, D.V., Krivolutskaya, N.A., Petrunin, A.G., Arndt, N.T., Radko, V.A., Vasiliev, Y.R., 2011. Linking mantle plumes, large igneous provinces and environmental catastrophes. Nature 477, 312–316. https://doi.org/10.1038/nature10385.

Solano, J.M.S., Jackson, M.D., Sparks, R.S.J., Blundy, J.D., Annen, C., 2012. Melt segregation in deep crustal hot zones: a mechanism for chemical differentiation, crustal assimilation and the formation of evolved magmas. J. Petrol. 53, 1999–2026. https://doi.org/10.1093/petrology/egs041.

Stelten, M.E., Cooper, K.M., Vazquez, J.A., Reid, M.R., Barfod, G.H., Wimpenny, J., Yin, Q. zhu, 2013. Magma mixing and the generation of isotopically juvenile silicic magma at Yellowstone caldera inferred from coupling 238U-230Th ages with trace elements

and Hf and O isotopes in zircon and Pb isotopes in sanidine. Contrib. Mineral. Petrol. 166, 587–613. https://doi.org/10.1007/s00410-013-0893-2.

Stelten, M.E., Cooper, K.M., Wimpenny, J.B., Vazquez, J.A., Yin, Q.Z., 2017. The role of mantle-derived magmas in the isotopic evolution of Yellowstone's magmatic system. Geochem. Geophys. Geosyst. 18, 1350–1365. https://doi.org/10.1002/2016GC006664.

Szymanowski, D., Ellis, B.S., Bachmann, O., Guillong, M., Phillips, W.M., 2015. Bridging basalts and rhyolites in the Yellowstone-Snake River Plain volcanic province: the elusive intermediate step. Earth Planet. Sci. Lett. 415, 80–89. https://doi.org/10.1016/j.epsl.2015.01.041.

Szymanowski, D., Ellis, B.S., Wotzlaw, J.F., Buret, Y., von Quadt, A., Peytcheva, I., Bindeman, I.N., Bachmann, O., 2016. Geochronological and isotopic records of crustal storage and assimilation in the Wolverine Creek–Conant Creek system, Heise eruptive centre, Snake River Plain. Contrib. Mineral. Petrol. 171, 106. https://doi.org/10.1007/s00410-016-1314-0.

Taylor, H.P., 1968. The oxygen isotope geochemistry of igneous rocks. Contrib. Mineral. Petrol. 19, 1–71. https://doi.org/10.1007/BF00371729.

Taylor, H.P., Sheppard, S.M.F., 1986. Igneous rocks: I. Processes of isotopic fractionation and isotopic systematics. Rev. Mineral. 16, 227–272.

Troch, J., Ellis, B.S., Mark, D.F., Bindeman, I.N., Kent, A.J.R., Guillong, M., Bachmann, O., 2017. Rhyolite generation prior to a yellowstone supereruption: insights from the Island Park-Mount Jackson rhyolite series. J. Petrol. 58, 29–52. https://doi.org/10.1093/petrology/egw071.

Troch, J., Ellis, B.S., Harris, C., Ulmer, P., Bachmann, O., 2018. The effect of prior hydrothermal alteration on the melting behaviour during rhyolite formation in Yellowstone, and its importance in the generation of low-$\delta^{18}O$ magmas. Earth Planet. Sci. Lett. 481, 338–349. https://doi.org/10.1016/j.epsl.2017.10.039.

Wagner, L., Forsyth, D.W., Fouch, M.J., James, D.E., 2010. Detailed three-dimensional shear wave velocity structure of the northwestern United States from Rayleigh wave tomography. Earth Planet. Sci. Lett. 299, 273–284. https://doi.org/10.1016/j.epsl.2010.09.005.

Watts, K.E., Leeman, W.P., Bindeman, I.N., Larson, P.B., 2010. Supereruptions of the Snake River Plain: two-stage derivation of low-??18O rhyolites from normal-??18O crust as constrained by Archean xenoliths. Geology 38, 503–506. https://doi.org/10.1130/G30735.1.

Watts, K.E., Bindeman, I.N., Schmitt, A.K., 2011. Large-volume rhyolite genesis in caldera complexes of the Snake River Plain: insights from the Kilgore Tuff of the Heise volcanic field, Idaho, with comparison to Yellowstone and Bruneau-Jarbidge rhyolites. J. Petrol. 52, 857–890. https://doi.org/10.1093/petrology/egr005.

Watts, K.E., Bindeman, I.N., Schmitt, A.K., 2012. Crystal scale anatomy of a dying supervolcano: an isotope and geochronology study of individual phenocrysts from voluminous rhyolites of the Yellowstone caldera. Contrib. Mineral. Petrol. 164, 45–67. https://doi.org/10.1007/s00410-012-0724-x.

Wotzlaw, J.F., Schaltegger, U., Frick, D.A., Dungan, M.A., Gerdes, A.G., Günther, D., 2013. Tracking the evolution of large-volume silicic magma reservoirs from assembly to supereruption. Geology 41, 867–870. https://doi.org/10.1130/G34366.1.

Wotzlaw, J.F., Bindeman, I.N., Watts, K.E., Schmitt, A.K., Caricchi, L., Schaltegger, U., 2014. Linking rapid magma reservoir assembly and eruption trigger mechanisms at evolved yellowstone-type supervolcanoes. Geology 42, 807–810. https://doi.org/10.1130/G35979.1.

Wotzlaw, J.-F., Bindeman, I.N., Stern, R.A., D'Abzac, F.-X., Schaltegger, U., 2015. Rapid heterogeneous assembly of multiple magma reservoirs prior to Yellowstone supereruptions. Sci. Rep. 5, 14026. https://doi.org/10.1038/srep14026.

Yuan, H., Dueker, K., Stachnik, J., 2010. Crustal structure and thickness along the Yellowstone hot spot track: evidence for lower crustal outflow from beneath the eastern Snake River Plain. Geochem. Geophys. Geosyst. 11. https://doi.org/10.1029/2009GC002787 (n/a-n/a).